

Interplay of classical and quantal descriptions of heavy-ion interactions*

Norman K. Glendenning

Lawrence Berkeley Laboratory, University of California, Berkeley, California 94720

Quasielastic collisions between complex nuclei, elastic, inelastic, and few-nucleon transfer are discussed both as a classical and quantal process. The classical trajectories can be used to illuminate the dependence of the quantal calculations on the physical parameters, and indeed can be used in a predictive way to suggest under what circumstances ambiguities can be resolved. The S -matrices for various quasielastic processes are exhibited and the quantal analog of the classical deflection function is compared with the classical one. The smooth behavior of the S -matrix for large angular momentum l suggests the possibility of a two-part approach where the lower l region is computed quantum mechanically, and the high- l region is either parametrized, treated semiclassically, or interpolated between widely spaced l 's. The much greater sensitivity of several-nucleon transfer reactions to the interior region compared to elastic and inelastic scattering is stressed. Various aspects of two-nucleon transfer are discussed, including multiple-step processes, their dependence upon collectivity of the intermediate states, and the opposite sense of the interference involved in pickup and stripping reactions to vibrational states.

CONTENTS

I. Introduction	659
II. The Potential	660
III. Critical Angular Momentum, Insensitivity to Imaginary Potential	661
IV. Deflection Function, Classical Conditions, Plunging Orbits, Grazing Peak	663
V. Elastic, Inelastic Scattering, and the Optical Potential	666
VI. Elastic Scattering for Large Coulomb Fields	667
VII. Two-Nucleon Transfer, Deep Orbits, Secondary Peaks	668
VIII. Quantal Analog of the Classical Deflection Function	672
IX. Indirect Transitions in Two-Nucleon Transfer, Opposite Behavior for Stripping and Pickup	676
X. Forward Angle Ripples, Uncertainty Principle	677
XI. Twofold Nature of Coulomb-Nuclear Interference	678
XII. Structure of the S -Matrix, Speculations on Future Developments	679
XIII. Summary	681
Acknowledgments	681
References	681

I. INTRODUCTION

Many of us who are now interested in heavy-ion reactions were earlier engaged in the study of reactions of light nuclides with nuclei. We learned that direct reactions could be described fairly accurately by the distorted wave Born approximation (DWBA) or its extension which includes coupling between some channels (CCBA). The theoretical description contains a number of parameters defining the optical potential, the bound state wavefunctions, and the interaction responsible for transitions. Their effect on the cross section generally had to be learned by

the "experimental" approach. Namely, a parameter was varied and its effect noted.

The point of view which I am going to elaborate on in this lecture is that for reactions between complex nuclei the classical trajectories can be used in a predictive way to suggest how and why the cross section depends on the parameters. Not only this, but the classical physics can be used to suggest what to look for and where, in order to answer specific questions. In the final stage of actually extracting the values of the physical parameters from an analysis of experiments, I believe one must ultimately rely on the full quantum description, *whenever* the nuclear force comes into play to a significant extent. Nevertheless, it is a fascinating aspect of heavy-ion reactions that the classical picture can be used to gain an understanding of many details of the cross sections and the underlying S -matrix that did not seem possible for nucleon or light nuclide reactions with nuclei. Perhaps a re-examination of these reactions will reveal that we could have obtained a more intimate understanding of them by a similar method. But that is not the subject of this paper.

I shall illustrate my discussion of heavy-ion interactions with calculations of elastic and inelastic scattering of $^{18}\text{O} + ^{120}\text{Sn}$, and the two-nucleon transfer reaction $^{120}\text{Sn}(^{18}\text{O}, ^{16}\text{O})$. I expect these examples to be typical of the phenomena associated with a large class of reactions and nuclei.

Near the end of the paper I will discuss briefly some possibilities for combining quantum and semiclassical or semiquantal means of calculating the S -matrix for heavy-ion reactions. A two part approach will be valuable at very high energies, or for truly massive projectiles, whenever many hundreds of partial waves are needed to describe the reaction.

* Work performed under the auspices of the U. S. Atomic Energy Commission. Based on a paper delivered at the International Conference on Reactions between Complex Nuclei, Nashville, Tennessee, June 10-14, 1974. *Proceedings of the International Conference on Reactions between Complex Nuclei*, Nashville, Tennessee, 1974, Vol. 2, Invited papers, Eds. R. L. Robinson *et al.* (North-Holland Publishing Company, Amsterdam, 1974), pp. 137-170.

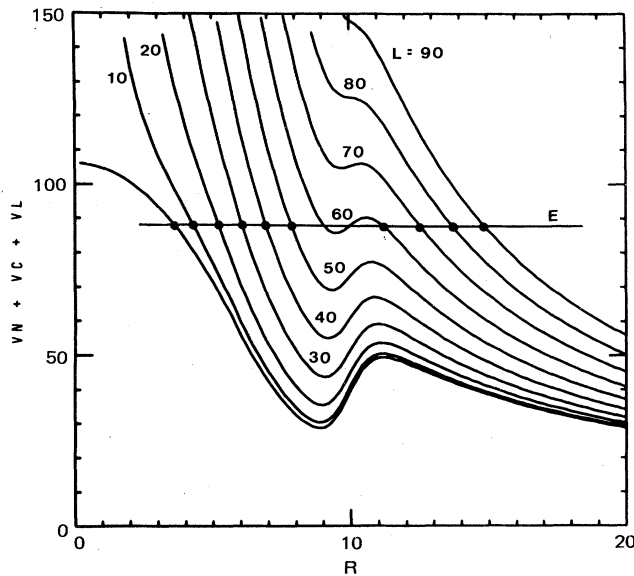


FIG. 1. For the system $^{18}\text{O} + ^{120}\text{Sn}$ and the potential of Table I the sum of the nuclear, Coulomb, and centrifugal potentials are shown for the values of angular momentum l indicated. The lowest curve, corresponding to $l = 0$, is the nuclear + Coulomb potential. The barrier is seen to be ~ 49 MeV. The horizontal line marks $E_{cm} = 87$ MeV, corresponding to a lab energy of 100 MeV. The turning points for various l are marked by dots. Note the discontinuity occurring at the critical $l_c \sim 57$.

II. THE POTENTIAL

The potential acting between two complex nuclei probably looks something like the lowest curve in Fig. 1. We acknowledge that when two complex nuclei overlap appreciably, many and complex changes can occur. Clearly for many purposes one can no longer consider the interaction potential to be describable as merely a function of the separation of their centers. Changes may occur in the shape, for example. Nevertheless, although it is undoubtedly exceedingly difficult to do, one can imagine that the wavefunction for the system is expanded on some basis of two-center wavefunctions in the absence of a mutual interaction, and that the substitution of such a wavefunction into the complete Hamiltonian would lead to a system of coupled equations. One can further conceptualize the elimination of most of these equations save those describing the elastic and a few other channels. The elimination leads, as is familiar, to the appearance of an effective potential in the remaining equations, which contains, as its first term, the original potential, and a second term which carries the effect of the eliminated channels on those that have been retained. The first term corresponds to the potential obtained by "freezing" the internal degrees of freedom and evaluating the potential energy acting between the two nuclei from the elementary interaction between nucleons or other variations of this procedure. Such potentials are often known under the

TABLE I. Potential parameters (energy in MeV, length in F).

V_0	r_0	a	r_c
-40	1.31	0.45	1.2

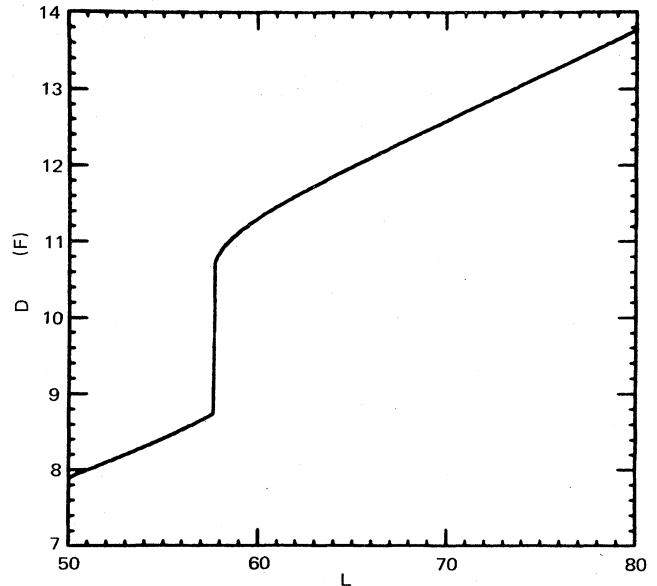


FIG. 2. The variation of the penetration depth or distance of closest approach D as a function of angular momentum for 100 MeV lab energy $^{18}\text{O} + ^{120}\text{Sn}$. The nuclear potential is that of Table I.

name of "folded interactions" which we should prefix by "frozen configuration." At distances for which appreciable overlap of the two densities occurs, such a folded potential will develop a repulsion, both because of the exclusion principle and because the nucleon-nucleon force saturates at the *normal* nuclear density. What is the behavior of the second term? From the procedure outlined above, we may never know. The optical potential for the nucleon-nucleus system is hard enough to calculate from first principles.

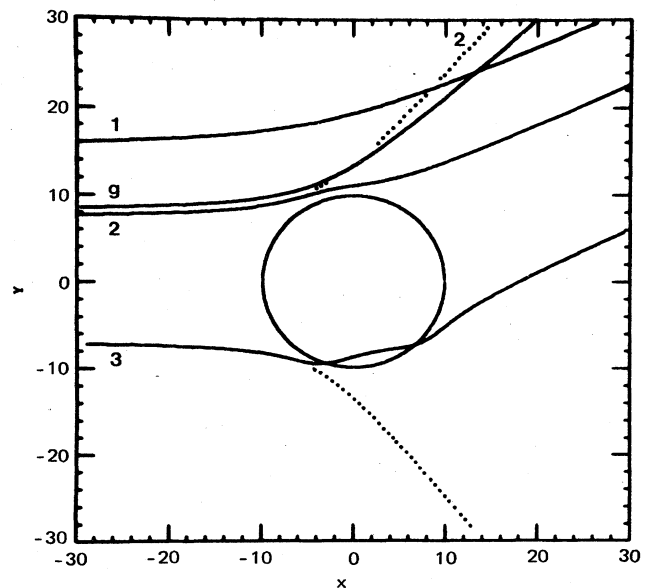


FIG. 3. Four classical orbits in the potential of Table I are plotted, three of which, having impact parameters 1, 2, and -3 ($3 < 2$) scatter to the same angle θ . The orbit g is the grazing one. The circle marks the half-value of the Woods-Saxon nuclear potential. The orbits are for ^{18}O scattered by ^{120}Sn at 100 MeV lab energy. Dotted lines show pure Coulomb orbits. The scale is in Fermi.

Can we learn anything from a different procedure than the frozen configuration folding? Some interactions have been computed under the assumption that the nuclear shapes are allowed to adjust so as to minimize the potential energy at each distance of separation. This adiabatic procedure does not lead to a short range repulsion because there is no buildup of density, and the Pauli principle is presumed to be satisfied as a result of the changes in shape. It is only one of many adiabatic potentials, others corresponding to excited intrinsic states of the deformed system. All of them *do* correspond to intrinsic excitations (many and complicated) with respect to the original ground state configurations of the separated nuclei. It may be that such adiabatic potentials are related to the *second* term of the effective interaction. The relationship, if it exists, is not clear.

If this discussion serves no other purpose, it at least underlines the fact that regardless of whether we can ever calculate it, an *effective* interaction can be considered to govern the motion of two complex nuclei when attention is focused on a few quasielastic channels (elastic and several inelastic and few-nucleon transfer channels). Perhaps its *real* part can be represented by the *local* potential shown in Fig. 1. Moreover, its first term, which is both real and local, corresponds to a frozen configuration folded potential. What we do not know is how strongly and in what way the first part is modified by the coupling to other channels. It may be that the potential is so strongly nonlocal and complicated in form for substantial overlap of the nuclei that no simple parametrizations such as discussed here are applicable. However, we have no reasonable alternative but to see how far a simple description can be carried, and elaborate or abandon it only as clearly require by the data.

From here on, we assume that the real part of the interaction has roughly the form shown, and will take as one of our goals to suggest how it might be determined from experiments. The actual potential shown is the sum of a Coulomb potential

$$V_c(r) = \begin{cases} \frac{ZZ'e^2}{r}, & r > R_c \\ \left[3 - \left(\frac{r}{R_c} \right)^2 \right] \frac{ZZ'e^2}{2R_c}, & r < R_c \end{cases} \quad (1)$$

and a nuclear potential which for the present we represent by a Woods-Saxon form

$$V_N(r) = \frac{V_0}{1 + \exp[(r - R)/a]}, \quad (2)$$

where

$$R_c = r_c A_2^{1/3}, \quad (A_1 < A_2), \quad \text{and} \quad R = r_0(A_1^{1/3} + A_2^{1/3}). \quad (3)$$

The parameters for the potential that we use for illustration are listed in Table I. This potential was found by Becchetti (1972) to reproduce some heavy-ion data.

With this choice, three regions of the potential can be identified, the long tail which is purely Coulombian, the

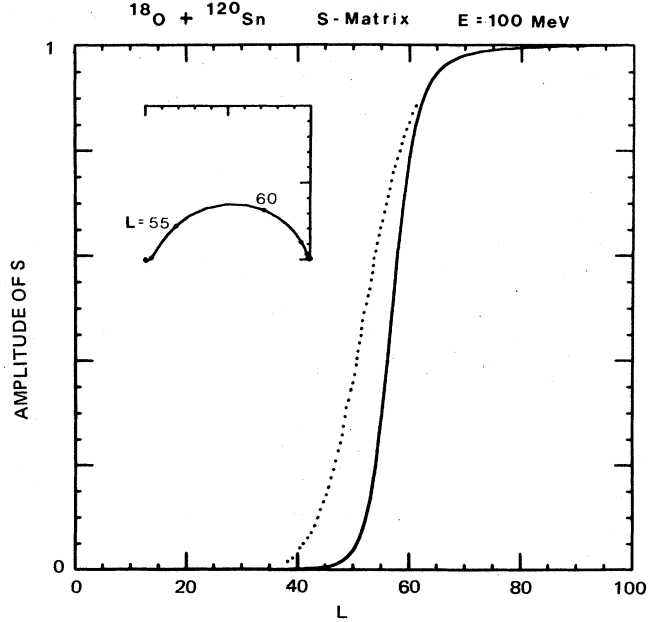


FIG. 4. The amplitude and phase (inset) of the *S*-matrix for elastic scattering of 100 MeV $^{18}\text{O} + ^{120}\text{Sn}$ corresponding to the potential of Table I and $W = 15$ MeV. Effect of coupling to the 2^+ state in Sn is included. The half-value occurs at $l \sim 57$, the critical angular momentum which is determined by the real potential. Dashed line corresponds to $V_0 = 0$ and shows by comparison how the real potential sucks high angular momentum orbits into the absorbing region. The inset shows *S* plotted in the complex plane, its real part on the *x* axis. The points which represent it are joined by straight lines. The position of $l = 55$ and 60 are marked.

attractive region just inside the barrier, and the repulsion at short distance, which under the above choice is Coulombian, but could contain a nuclear repulsion, as would a frozen configuration folded potential.

III. CRITICAL ANGULAR MOMENTUM, INSENSITIVITY TO IMAGINARY POTENTIAL

The simplest classical scattering quantity that can be defined is the distance of closest approach that the system will achieve, given its energy and angular momentum (or equivalent to the latter, the impact parameter $b = l/k$). The various curves of Fig. 1 above the lowest one correspond to

$$V_l(r) = V_N(r) + V_c(r) + l(l+1)\hbar^2/2mr^2 \quad (4)$$

the sum of the potential plus centrifugal energy for a few values of l . The outer intersection of each of these with a horizontal line drawn at the height of the *center-of-mass* energy gives the closest distance for that value of l . This is illustrated for one energy E . Of particular importance is the *discontinuity* in the distance of closest approach, or *penetration depth* D as a function of l . This discontinuity occurs at l_c , the critical angular momentum for which, at the given energy, the barrier in V_l is just surmounted, as illustrated in Fig. 1. For all values $l < l_c$, D increases slowly with l but jumps discontinuously to a larger value as l crosses l_c to larger values.

The discontinuity in D (see Fig. 2) has a very significant consequence. Trajectories with $l > l_c$ remain "outside" the

$$^{18}\text{O} + ^{120}\text{Sn} \quad E = 100 \text{ MeV}$$

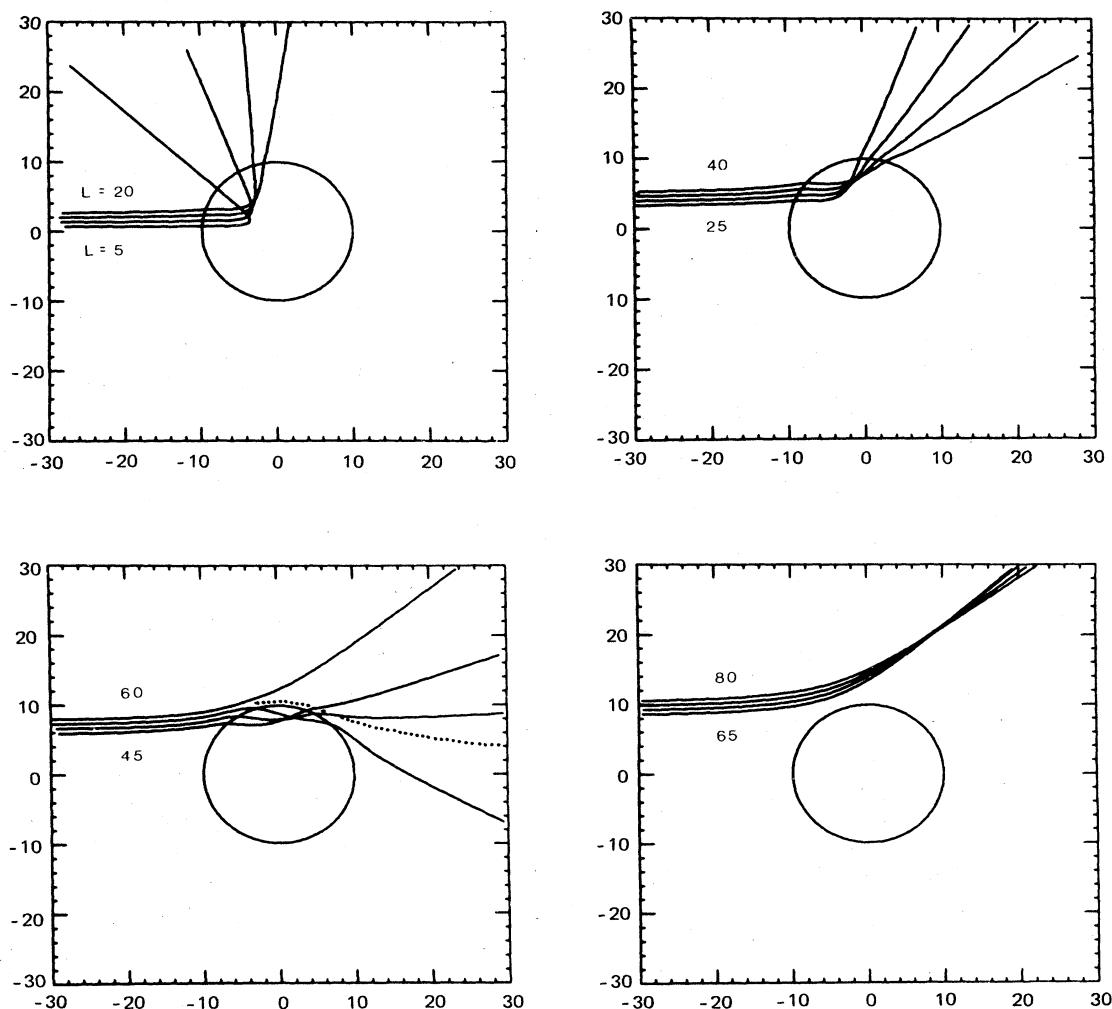


FIG. 5. Some trajectories in the potential of Table I, at intervals of $l = 5$ for 100 MeV ^{18}O scattered from ^{120}Sn . The circle marks the half-value of the nuclear potential. An additional skimming orbit is shown by dotted line.

nucleus, while those with $l < l_c$ plunge deeply in. For the typical energy shown, there is *no intermediate* situation. This is illustrated by some trajectories in Fig. 3 showing a Coulomb one, a skimming one, and a plunging one. Those that do plunge traverse a considerable length of the nuclear medium, of the order of a nuclear radius or more. Because of their long path length in the medium they suffer strong attenuation from the elastic flux, almost independent of how deep the imaginary potential is. The point is well emphasized by one of Shakespeare's characters who, having been fatally stabbed, speaks of his wound, "tis not so deep as a well, nor so wide as a church door; but tis enough, twill serve" (Shakespeare, 1599). Thus we understand the insensitivity to W encountered in optical model searches. We also learn that the sharp cutoff of the elastic S -matrix at l_c (Fig. 4) is determined by the *real* potential whenever it is strong enough to produce a net attraction, because the *real* part of the

potential acts to deflect particles deeply into the nucleus, or not all (see Figs. 3 and 5). In the absence of the real potential, the S -matrix cuts off much slower. Only for very weak real potentials does the location of the cutoff in S reflect the profile of the imaginary potential.

In Fig. 4 the critical angular momentum corresponds very closely with the half-value of the S -matrix. For very short wavelength collisions, typical of heavy ions, S is a *smooth* function of l . The reason for this will be given shortly. We want at this point to note that the elastic scattering is characterized by such a simple function as shown, and its phase is also simple (Blair, 1957). The symmetry about l_c is only approximate, and accidental. Above l_c , the approach to unity is governed by the quantum mechanical penetration of the barrier, and the coupling to inelastic channels, especially as occurs through the long range Coulomb potential. The approach to zero

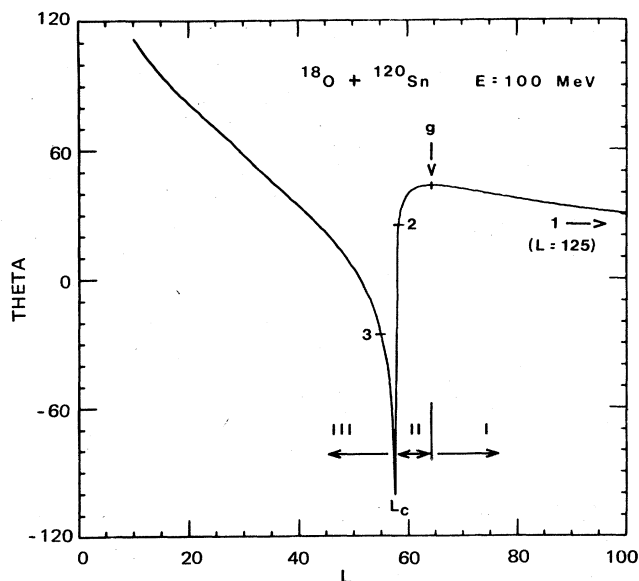


FIG. 6. Deflection function from which the classical scattering angle of a trajectory with angular momentum l can be read for 100 MeV $^{18}\text{O} + ^{120}\text{Sn}$. Points on the function corresponding to the four orbits of Fig. 3 are marked. The back scattering for small l is caused by the repulsive Coulomb core, Fig. 1, which at this energy is not surmounted. The singularity occurs at the critical angular momentum l_c . The three regions I, II, and III are discussed in the text. The grazing angle θ_g , which is the maximum to which nonpenetrating orbits can scatter, is about 43° .

below l_c is slower than would occur classically (sharp cutoff at l_c) because of the quantum mechanical reflection at the edge of the barrier.

Because (Blair, 1957) of the strong absorption of trajectories with $l < l_c$, elastic scattering is expected to yield information about the interaction at best into distances corresponding to the penetration depth $D(l)$ for values of $l > l_c$. The smallest of these is $D(l_c)$. This decreases only very slowly with energy, once the energy exceeds the Coulomb barrier, so that elastic scattering carried out at higher energy does not achieve much headway in probing deeper. Now I said that at best elastic scattering probes as deep as $D(l_c)$. In fact, it turns out that elastic scattering does not probe this deep with sufficient sensitivity to determine the nuclear potential there. This will be elaborated later.

IV. DEFLECTION FUNCTION, CLASSICAL CONDITIONS, PLUNGING ORBITS, GRAZING PEAK

We saw some typical trajectories in Fig. 3 and others are shown in Fig. 5. For some purposes it is useful to make a plot of their scattering angle versus the angular momentum or, equivalently, the impact parameter. A few points on such a plot, which is called a deflection function, could be read from the trajectories. We show such a deflection function in Fig. 6, which corresponds to 100 MeV laboratory energy $^{18}\text{O} + ^{120}\text{Sn}$ scattered from the potential shown at the bottom of Fig. 1. The location of the four orbits of Fig. 3 is marked. Three of them were especially chosen to show how different orbits in a potential such as that acting between heavy ions (Fig. 1) can scatter to

the same angle (Ford and Wheeler, 1959). This introduces some very special features into the cross sections, as we shall discuss later on.

Classically, l can have any value, integer and noninteger, but in quantum mechanics only integer values are allowed. We see that for oxygen the deflection function is sampled at very small intervals. This is in contrast to a typical proton reaction. Figure 7 shows a deflection function for 30 MeV protons on ^{120}Sn . Here we see that integer angular momenta sample the deflection function very sparsely. This very relevant fact, necessary to make sense of a classical discussion of scattering, has not apparently been noted previously. Only when the density of angular momentum states per unit impact parameter ($L/b = k$) is large does the classical discussion become useful. I use the word useful so as to avoid implying that a classical description is quantitatively valid. For deflection functions like those shown, classical mechanics is not quantitatively valid because large changes in θ occur between neighboring angular momentum states in the vicinity of $l = l_c$. This means that a wave packet would be broken up by the action of the nuclear field near this angular momentum, and scattered in all directions.

Thus classical, or semiclassical, methods cannot be expected to be more than qualitatively valid whenever the nuclear force is involved appreciably if it is strong enough to produce sharp changes in θ_l . As we shall see in our later discussion, elastic, inelastic, one-particle transfer, and two-particle transfer are sensitive to increasingly smaller distances, i.e., to the region where the nuclear force is strong. Semiclassical calculations, therefore, become increasingly unreliable for the above sequence of interactions, except of course for energies below the Coulomb barrier. The exception is a drastic one, since it excludes most of the interesting physics.

However, the interest in the classical description is here qualitative. As I stated in the introduction, I want to

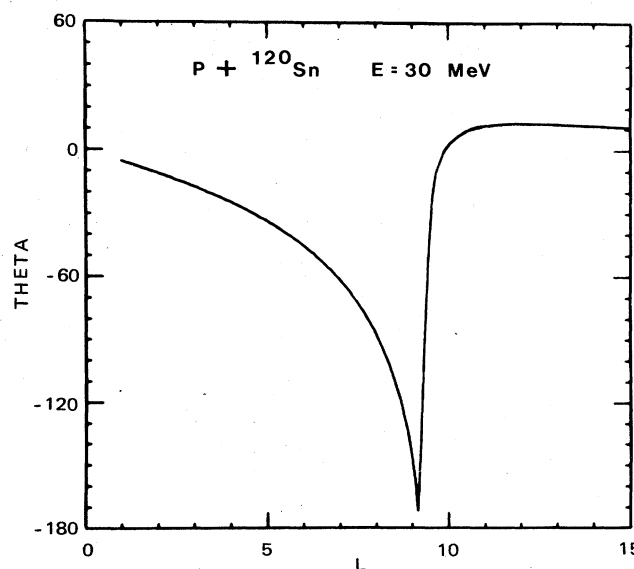


FIG. 7. Deflection function for 30 MeV protons scattered by ^{120}Sn , using the potential $V = -57$, $r_0 = 1.13$, $a = 0.744$.

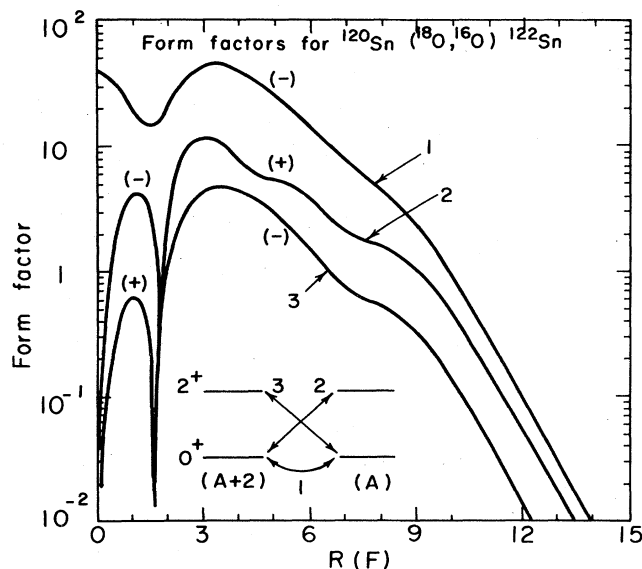


FIG. 8. The $L = 0$ and $L = 2$ form factors for two-nucleon transfer in the reaction $^{120}\text{Sn}(^{18}\text{O}, ^{16}\text{O})^{122}\text{Sn}$ or its inverse. Absolute value is plotted and signs are indicated.

use it to understand the dependence of cross sections on the physical parameters. Such an understanding can be used to suggest what kind of experiments to do. The actual analysis must be done quantum mechanically.

At an earlier point I stated that we expect a *smooth* behavior of the S -matrix as a function of l when the de Broglie wavelength is short enough. The reason for this is clearly connected with the density of integer angular momentum states on the deflection function.

We identified three classes of orbits and illustrated one from each class in Fig. 3, and we now identify the region of the deflection function (Fig. 6) to which they correspond. Region I corresponds to orbits which turn away from the nucleus, because of the repulsive Coulomb field. However, the lower l orbits of this region do come into the tail region of the nuclear field and are not deflected to as large an angle as they would have been in a pure Coulomb field. The opposite effects of the two fields produces the situation characterized by the grazing orbit l_g , which scatters to the maximum angle possible for nonpenetrating orbits. This orbit marks the boundary with region II. The nuclear attraction causes the orbits of this region to *skim* the edge of the attractive region. The critical angular momentum, l_c , marks the point where the deflection function has a singularity. Since l_c corresponds to the top of the barrier where the net radial force is zero, it corresponds to a capture (though unstable) orbit. Trajectories with l very close to l_c spiral around the nucleus. The skimming orbits of region II are in sharp contrast with the plunging orbits of region III below l_c , such as 3 in Fig. 3. The plot of the penetration depth D in Fig. 2 clearly shows the discontinuity between these orbits and others.

The maximum in the deflection angle for nonpenetrating orbits, marked by g , is a prominent feature of the deflection function and provides an understanding of angular distributions. The original explanation for the grazing

angular distribution was based on the notion of pure Coulomb orbits and is therefore deficient. According to that explanation, close orbits scatter to large angles but are absorbed, while distant orbits scatter forward but do not very successfully cause transitions because of the distance between the nuclei. Between is an optimum orbit which defines the grazing peak. *Instead* we see that it is the attractive nuclear field, counterbalancing the repulsion of the Coulomb, that produces a *maximum* scattering angle for nonpenetrating orbits. This we call the grazing angle. Some of the penetrating orbits can scatter *both* forward or back of this angle but suffer attenuation by absorption, while more distant orbits which scatter only forward of the grazing angle contribute little to reactions because of the distance between the nuclei.

It might at first be imagined that the trajectories of region III do not contribute at all to heavy-ion reactions because of strong absorption. However, the absorption of such close orbits may be offset by other factors. Although the trajectories and deflection functions refer to classical *elastic* scattering, we consider them relevant to other quasielastic processes in which the exchange of energy, mass, charge and angular momentum are all *relatively* small (i.e., $\Delta E/E \ll 1$, etc.). Such processes include inelastic scattering and one or several nucleon transfer reactions all leading to low-lying states. For the purpose of this qualitative discussion we suppose that the trajectory is undisturbed and that the cross section for any of the quasielastic processes can be estimated from three factors. One factor is the intrinsic elastic cross section, as estimated here from the classical deflection function. Flat regions of $\theta(l)$ indicate the scattering of many trajectories to nearly the same angle and give rise therefore to a large cross section. The other two factors are the absorption into other channels represented in the quantum calculations by the imaginary potential, and lastly the form factor for the particular quasielastic process. We can get an appreciation for the various regions of sensitivity of quasielastic processes from their form factors in r space. Thus for inelastic, one- and two-nucleon transfer, these form factors behave, at large distance, like

$$F_{\text{inel}}(r) = -\beta R \frac{\partial V}{\partial r} + \beta_c \frac{3Z_1 Z_2 e^2 R_c^L}{2L+1 r^{L+1}}, \quad r > R_c,$$

$$F_1(r) \rightarrow \exp[-(2mB_1/\hbar^2)^{1/2} r],$$

$$F_2(r) \rightarrow \exp[-(4mB_2/\hbar^2)^{1/2} r]. \quad (5)$$

In the above, β and β_c are the nuclear and charge deformations, respectively, and R is the radius of the vibrating nucleus, while B_1 and B_2 are the binding energies of one and two nucleons. The latter two expressions approximate the behavior in the tail region. Actual computed

TABLE II. Estimate of the relative contribution of orbits 2 and 3 of Fig. 3 to two-particle transfer.

	Probability of survival	Transfer probability	Elastic cross section	Product
Orbit 2	e^{-2}	e^{-8}	1	e^{-10}
Orbit 3	e^{-12}	1	e	e^{-11}

form factors for two-nucleon transfer are shown in Fig. 8 (Ascuitto and Glendenning, 1973a and 1973b). In the order listed the above processes are increasingly concentrated in the nuclear region, and thus will exhibit an increasing sensitivity to the interaction at small distance. Thus, although the penetrating orbits of region III are subject to strong loss to other more complicated channels (for which we sometimes use the word absorption, not meaning to imply, however, compound nucleus formation), nonetheless, a process such as two-nucleon transfer to a coherent state *strongly* prefers the deep penetration. Whether this region manifests itself in a particular case depends on how the three factors balance out.

We make a very crude estimate now of the relative contributions of orbits 2 and 3 of Fig. 3 to two-nucleon transfer. To estimate the absorption we note that the decay length in a semi-infinite medium is given by the reciprocal of the imaginary part of the wave number. In this application we compute a typical *local* value for the orbit in question and use a rough estimate of the path length in the absorptive region, read from Fig. 3. The wave number is

$$K \simeq \left[\frac{2m}{\hbar^2} (E - V) \right]^{1/2} \left(1 - \frac{i}{2} \frac{W}{E - V} \right) \quad (6)$$

which is roughly $6(1 + i/8)F^{-1}$. Thus the amplitude decreases as $\exp(-3r/4)$. The path length of orbit 3 is almost $8F$. Orbit 1 is outside in the tail region of $W(r)$; we give its amplitude to be attenuated by about $1F$ path length or e^{-1} . From Fig. 8 the form factor is approximately e^{-r} in the region in question, which appears squared in the cross section. Finally the elastic cross section is

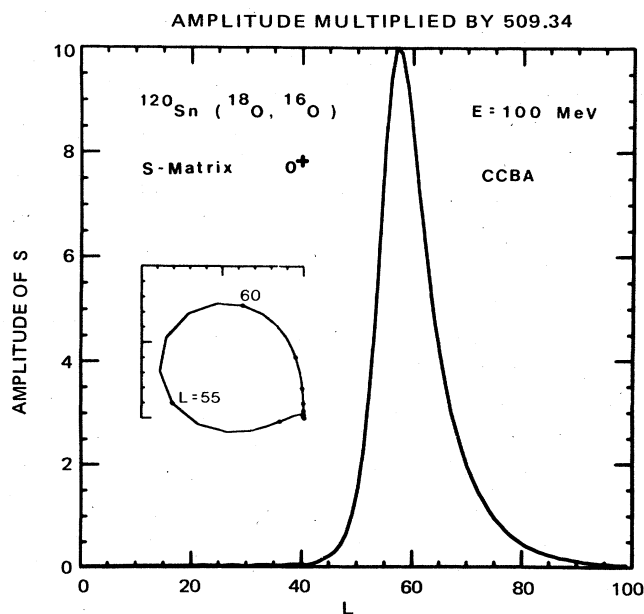


FIG. 9. The amplitude of the S-matrix for the ground state transition in the reaction $^{120}\text{Sn}(^{18}\text{O}, ^{16}\text{O})^{122}\text{Sn}$ at $E = 100$ MeV. The inset shows S plotted in the complex plane, its real part on the x axis. Points representing S are joined by straight lines, and its position at $l = 55$ and 60 are marked. It begins and ends at the origin.

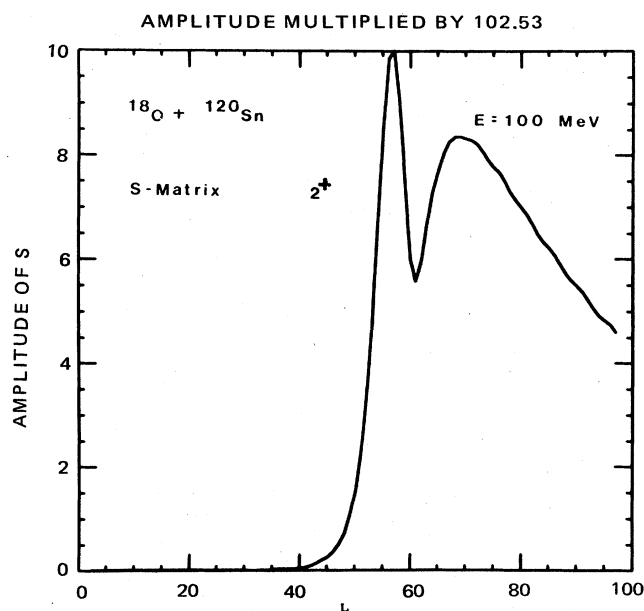


FIG. 10. The amplitude of the S-matrix corresponding to the inelastic excitation of the 2^+ vibrational state of Sn in the reaction $^{18}\text{O} + ^{120}\text{Sn}$. Actually three S 's occur for each incident l , corresponding to the three possible values of the final angular momentum l , $l \pm 2$. The one for $l' = l$ is shown, being typical. The lower peak is dominated by the nuclear field, while the upper one, which extends to very high l , is dominated by the Coulomb field. The minimum arises from a destructive interference between the two for l in the vicinity of 62.

given classically for angular momentum l by

$$\left(\frac{d\sigma}{d\Omega} \right)_l = \chi^2 \frac{(l + \frac{1}{2})}{\sin \theta} \left| \frac{d\theta}{dl} \right|^{-1} \quad (7)$$

The three factors for each orbit are collected in Table II. We see that for two-nucleon transfer the two close orbits are within a factor e in importance, revealing that the contribution of penetrating orbits is by no means negligible. Of course we must rely in the final analysis on a quantum calculation. The quantity which will illustrate our point is the absolute value of the S-matrix plotted as a function of angular momentum. The S-matrix gives the amplitude in the outgoing channel to which it corresponds, given that the flux in the incident channel is unity. Thus, for example, the partial cross section for given l is

$$\sigma_l = \frac{\pi}{k^2} (2l + 1) |S_l|^2, \text{ nonelastic} \quad (8)$$

Using the potential of Table I and the form factor of Fig. 8, we compute the S-matrix for two-nucleon transfer to the ground state for the reaction $^{120}\text{Sn}(^{18}\text{O}, ^{16}\text{O})^{122}\text{Sn}$, $E = 100$ MeV lab. The result, shown in Fig. 9 shows a very smooth narrow function of l centered at $l = 57$ which is the critical angular momentum for this potential at this energy, as was seen in Figs. 1, 2, and 6. The S-matrix at the values of $l = 55$ and 58 , which correspond approximately to orbits 2 and 3, the skimming and plunging orbits of Fig. 3, are seen to be comparable, confirming the expectation formed by the above crude estimate.

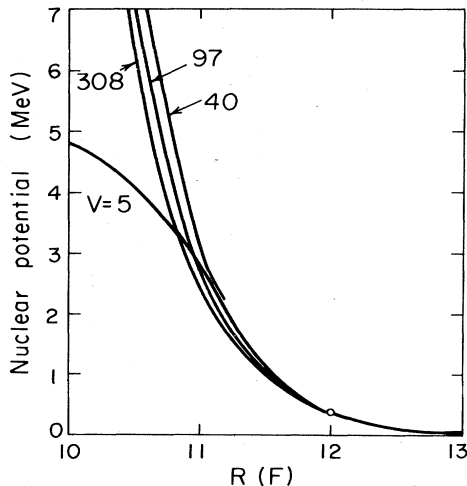


FIG. 11. The tail region of the real part of potentials which, together with the imaginary parts listed in Table III, yield elastic cross sections which are indistinguishable. The central value of the depth is in each case indicated and can be used to identify the corresponding entry in Table III. These are members of a continuum of potentials. Here V can have any value lying between these curves, and possibly beyond.

The above case in which the reaction region is confined to a very narrow band of orbits is in marked contrast to the inelastic scattering to the collective 2^+ state in the entrance channel of the above reaction. Its S -matrix, shown in Fig. 10, reveals the very large contribution of the high- l region, corresponding to the very slow fall off of the electric quadrupole part of the field. It will be noted that the S -matrices for the two cases are cut off at the same $l_3 = 54$, at least for the absorption strength used here, which is consistent but not very well determined by elastic scattering. Nevertheless, the two-nucleon transfer is more sensitive to close distances perhaps up to the penetration depth (Fig. 2) for l_3 . This is so because the

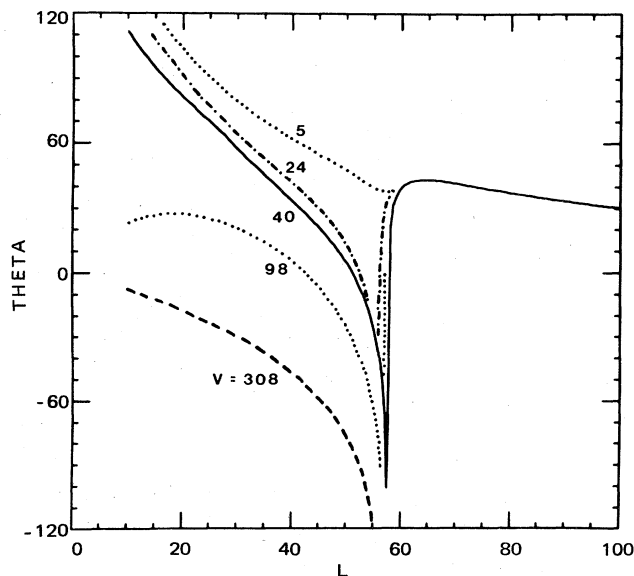


FIG. 12. Deflection function for 100 MeV $^{18}\text{O} + ^{120}\text{Sn}$ corresponding to the potentials whose tails are plotted in Fig. 11 and whose full parametrization can be found in Table III. They are identical beyond $l \sim 60$.

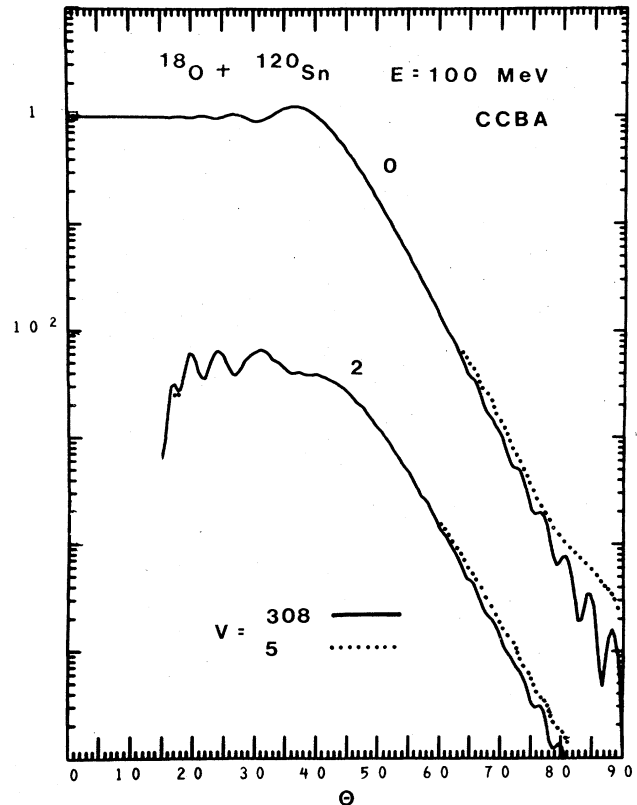


FIG. 13. Elastic and inelastic 2^+ cross sections for 100 MeV $^{18}\text{O} + ^{120}\text{Sn}$ cannot distinguish between the two extreme potentials of Table III (first and last entry). The two scales refer to the two curves. For the inelastic cross section, our calculation for $\theta \leq 15^\circ$ is inaccurate because only the contributions for $l \leq 215$ and $R \leq 30F$ were computed at this energy. Cross sections throughout are in mb/sr.

relative contribution of this orbit is bigger than in the case of inelastic scattering.

The above discussion reveals that, depending upon the particular reaction, we can select the sensitivity to various orbits and hence to reaction regions. In addition, further fine tuning for a given reaction can be achieved by selecting the angle region.

V. ELASTIC, INELASTIC SCATTERING, AND THE OPTICAL POTENTIAL

It is widely said that elastic scattering is sensitive only to the tail region of the potential. Here we attempt to make this statement more precise. To do so we are motivated by the importance of the grazing angle as revealed in the deflection function. Classically this is the maximum angle to which nonpenetrating orbits can scatter. Presumably then this is the invariant that is possessed by all potentials which can be found to yield the same quantum elastic scattering. Therefore, we focus on the penetration depth $D(l_g)$ of the grazing orbit l_g . For the potential of Table I we read from Fig. 6 that $l_g \simeq 64$, and from Fig. 2 that $D(l_g) \simeq 12F$.

This is the distance at which we choose the real part of all our potentials to have the same value, which is only 0.36 MeV. The radius and diffuseness in each case

are chosen so that in a $1F$ neighborhood of this point the potentials do not differ radically, as illustrated in Fig. 11. The deflection functions for these potentials are shown in Fig. 12 and are all seen to have the same form in the neighborhood of l_0 and beyond. They do differ radically for smaller l . Nevertheless, in each case an imaginary potential can be found which yields quantum elastic cross sections, which are indistinguishable by typical experiments. Indeed in some cases two imaginary potentials are shown. The complete potentials are tabulated in Table III together with the standard one ($V = -40$). We emphasize that these potentials are only a selection from a continuum (see Fig. 11). From this fact we conclude that elastic scattering at best can be used to determine the potential only roughly in the vicinity of the penetration depth of the grazing orbit. How rough the determination is can be guessed from Fig. 11. Were it not for the fact that we need to know the interaction in order to calculate more complicated processes, we would dismiss the elastic optical potential with the comment that it is a very complicated and nonunique way of generating a very simple S -matrix, Fig. 4.

At this point we note, in case the hope is entertained that the cross section determined at several energies could be used to distinguish among the potentials, that $D(l_0)$ is almost constant, ranging from 11.6 to 11.8 F for E between 60 and 160 MeV. Therefore, over the range of energies from the barrier up to several times its value, the same region of configuration space dominates the

TABLE III. A selection from a continuum of potentials which yield elastic scattering cross sections which are indistinguishable for 100 MeV $^{18}\text{O} + ^{120}\text{Sn}$. Reaction cross sections are equal within $\sim 3\%$. In each case the Coulomb radius is $r_c = 1.2$. The 40 MeV potential is our standard one.

V	r_V	a_V	W	r_W	a_W	σ_R
-308	1.125	0.52	- 8.9	1.334	0.5323	1800
			-48.5	1.203	0.5216	
-214	1.125	0.55	- 8.18	1.348	0.5433	1820
-149	1.19	0.5	- 8.44	1.337	0.5224	1795
-98	1.22	0.5	- 7.404	1.354	0.4936	1785
			-33.34	1.232	0.5001	1745
-67	1.24	0.5	- 5.673	1.378	0.5119	1805
-40	1.31	0.45	-15	1.31	0.45	1760
-24	1.32	0.48	- 4.866	1.401	0.4631	1790
-10.7	1.39	0.45	- 8.063	1.385	0.4179	1780
-5.49	1.46	0.38	- 7.763	1.424	0.3276	1790

elastic cross section. This is confirmed by the calculations shown in Fig. 13 and Fig. 14 for $E = 100$ and 160 MeV, where elastic and inelastic scattering are compared for the two extreme potentials of Table III.

The inelastic cross sections¹ to the collective 2^+ state are also shown in these figures. It is disappointing to note that they are hardly more sensitive than elastic scattering. Moreover the differences, small as they are, are probably well within the uncertainty of the model for the vibrational state.

Under these circumstances we must look to other reactions and also to theory for guidance in determining the potential. Theoretical estimates must draw on the relevant aspects of our knowledge of nuclear forces, densities, and bulk properties of nuclei if they are to be credible (Randrup, Swiatecki, and Tsang, 1975).

VI. ELASTIC SCATTERING FOR LARGE COULOMB FIELDS

This work is based mainly on examples which are typical of many current experiments in which the projectile is fairly light and the energy is in the range between the Coulomb barrier and, say, twice the barrier. In such cases the energy intersects a pocket in the effective potential (Fig. 1).

An important difference occurs if the charges of the colliding nuclei are so large that the nuclear potential is unable to produce a pocket. This is almost the case, even for $^{40}\text{Ar} + ^{120}\text{Sn}$, as is shown in Fig. 15. An important consequence of the pocket is the existence of a large number of plunging orbits, as discussed in Sec. IV. This is dramatically illustrated in Fig. 2 where we see that the orbits stay outside $r \gtrsim 10.8F$ or they plunge interior to $r \lesssim 8.7F$. The collisions are either very peripheral or very penetrating. The latter orbits are of course strongly absorbed out of the elastic beam (Fig. 4).

¹ The radial integration in the calculations was carried to $30F$ at both energies and to $l = 215$ and $l = 295$ for $E = 100$ and 160 MeV, respectively. These conditions do not pick up all the Coulomb excitation. But since they do gather all of the nuclear excitation, our conclusions concerning the dependence on the nuclear field are not affected by the nonconvergence with respect to very distant collisions.

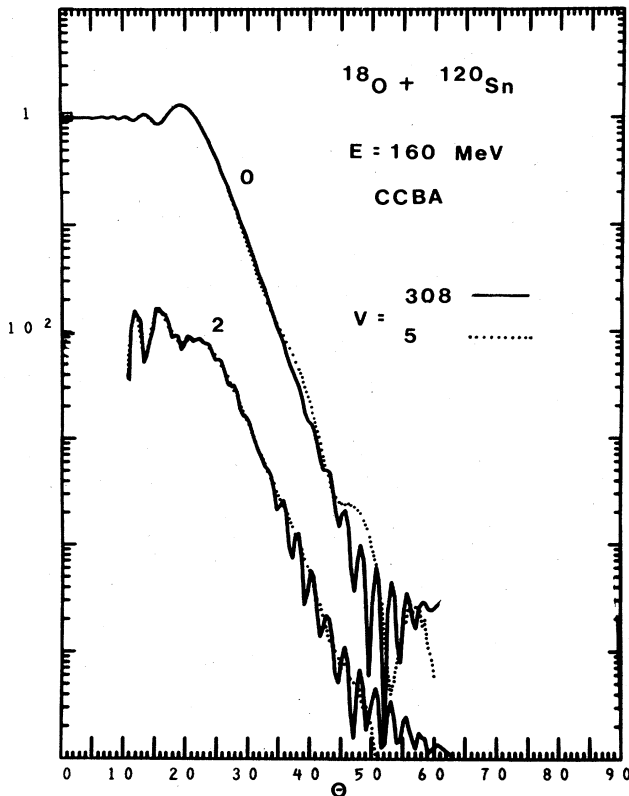


FIG. 14. Elastic and inelastic cross sections for 160 MeV $^{18}\text{O} + ^{120}\text{Sn}$ cannot distinguish between the two extreme potentials of Table III (first and last entry).

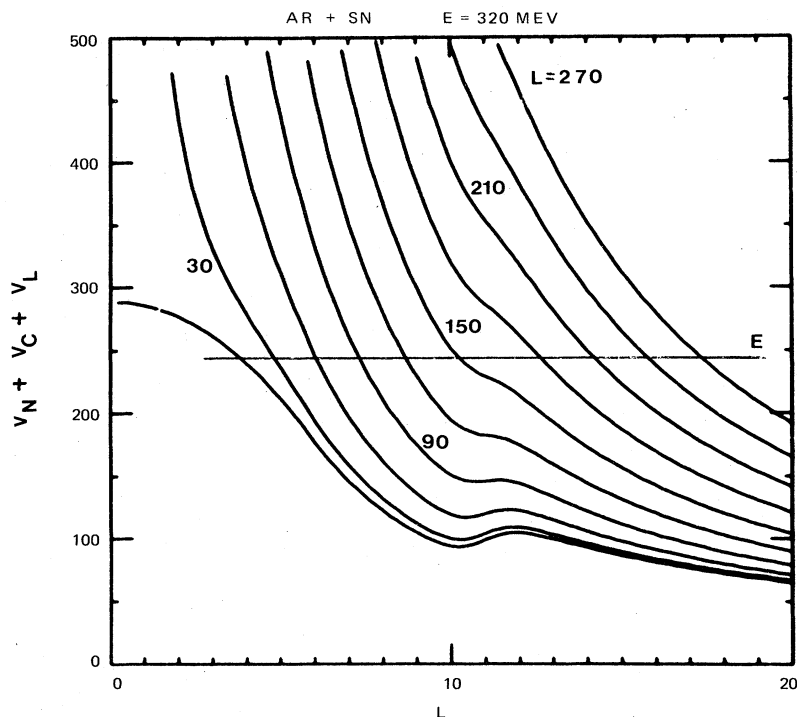


FIG. 15. For $^{40}\text{Ar} + ^{120}\text{Sn}$ and the potential of Table I the effective potential is shown. The center-of-mass energy is marked by a horizontal line. There is no discontinuity in the turning points at moderate energies above the barrier in contrast to Fig. 1.

If, in contrast, the charges are large enough to eliminate the pocket at the center of mass energy of the collision, as in Fig. 15, then the classical turning point suffers no

discontinuity. In this case there is a band of orbits which sample the *inner* edge of the interaction region without plunging into the interior. Consequently we can expect that the elastic scattering can now carry information at least to a distance where the potential is a few MeV deep. There is another fine distinction. We stressed earlier that while it is the absorption that causes the attenuation of the elastic S -matrix for $l < l_c$, it is the real part of the potential which determines the value of l_c whenever the center of mass energy intersects a pocket region of the effective potential. If the charges are large enough to eliminate the pocket then the critical angular momentum is *not* determined by the real potential but by the imaginary potential (as in the two cases shown in Fig. 4, for example). In contrast to the situation for light projectiles discussed in Sec. III, the elastic scattering of heavy projectiles should be quite sensitive to the imaginary potential geometry, for it now plays a principle role in determining the profile of the elastic S -matrix.

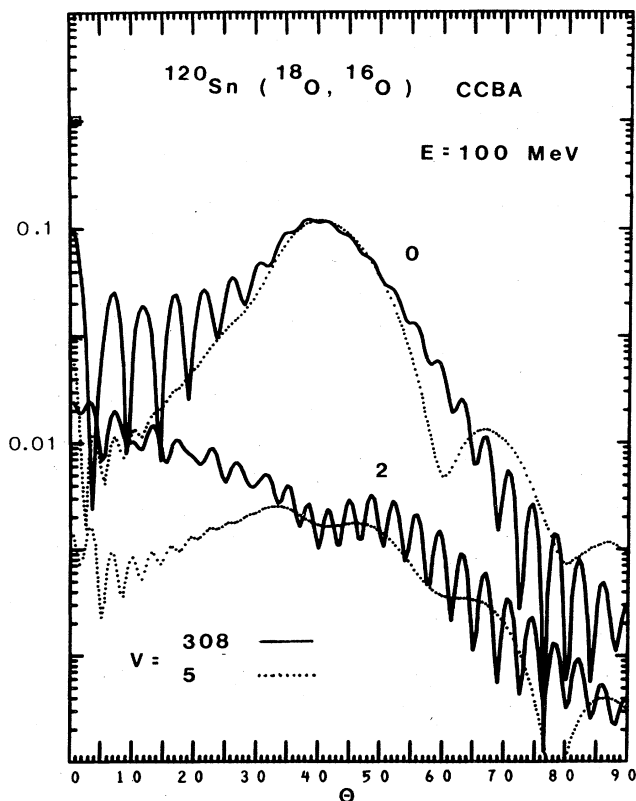


FIG. 16. Cross sections for two-neutron transfer to the ground and 2^+ vibrational state easily distinguish between the two extreme potentials of Table III. The two scales refer to the two states.

VII. TWO-NUCLEON TRANSFER, DEEP ORBITS, SECONDARY PEAKS

We have learned that elastic scattering yields very little information about the interaction between heavy ions. Earlier we discussed the form factors for various quasi-elastic processes, and stressed that several-nucleon transfer reactions prefer very close collisions. Indeed, the form factor is peaked at a separation distance of the centers corresponding to a total immersion of one nucleus within the other (Fig. 8). Whether the nuclei in such close collisions survive to emerge again in simple direct reaction channels with sufficient probability to be observed is as yet an unsettled question. If they do, they carry information about that region, and we must learn how to interpret it.

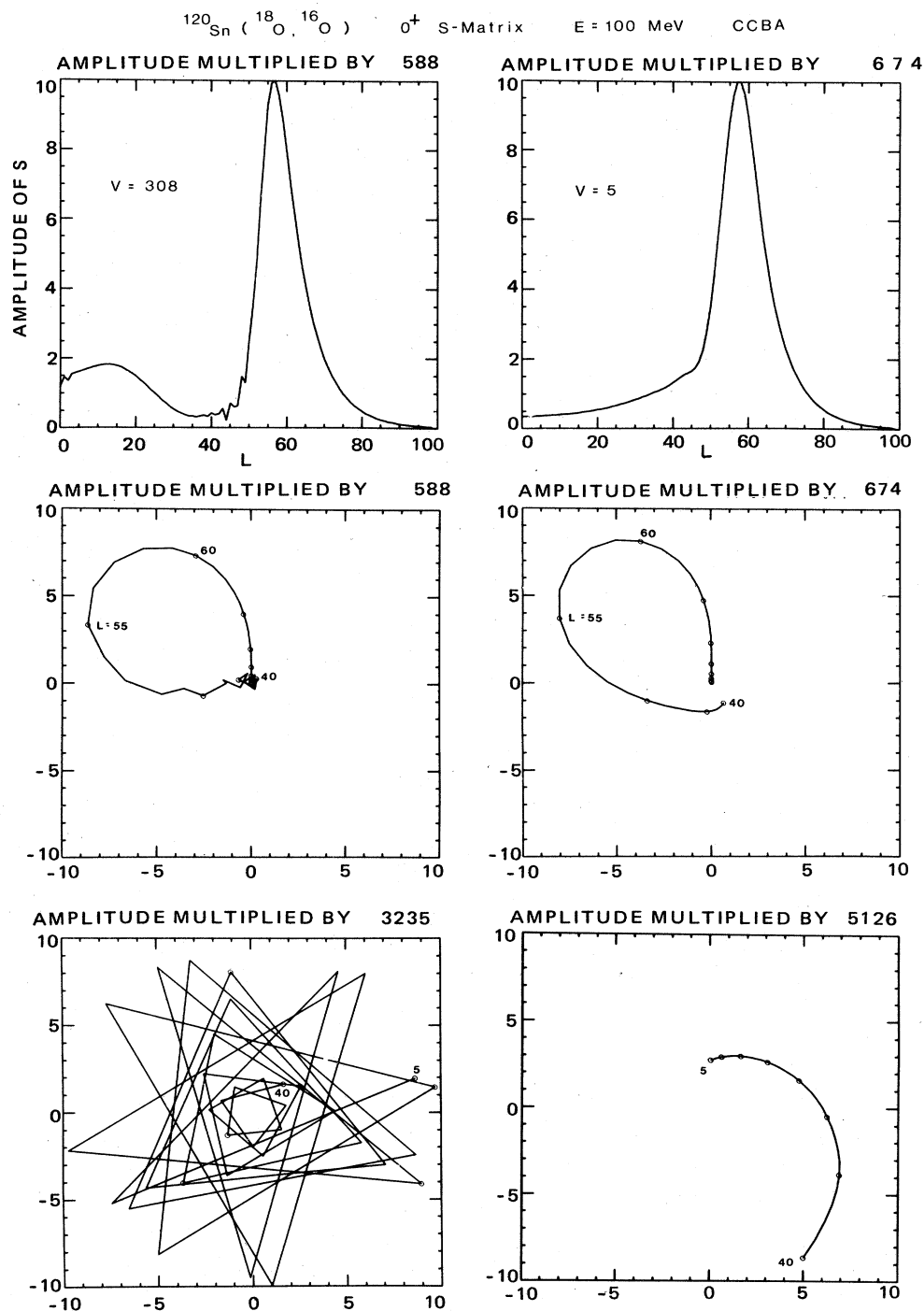


FIG. 17. The S -matrix for the ground state transfer are compared for the two extreme potentials of Table III. The corresponding cross sections are in Fig. 16. The amplitude of S is plotted in the top part of the figure, and S itself is plotted in the complex plane in the bottom part. Note the resonant behavior in the lower l region in the case of the deep potential, signaled by the rapid rotations.

For orientation we consider first the two extreme potentials of Table III, whose elastic and inelastic cross sections were compared at two energies in Figs. 13 and 14 and found to be indistinguishable under usual experimental conditions. In contrast, the two-neutron transfer cross sections leading to the ground and 2^+ states in ^{122}Sn are very different and easily distinguished at angles away

from the grazing angle (Fig. 16). At this point we emphasize that the grazing angle is ideal for determining spectroscopic information in transfer reactions because it depends so weakly on the interaction. However, it is only by making measurements away from the grazing angle that information about interior conditions can be determined. The S -matrices at $E = 100 \text{ MeV}$ for the ground

TABLE IV. The Becchetti and Morrison potentials and their reaction cross sections at two energies. The primed potentials have weaker absorption. Pairwise they have close to the same reaction cross sections. Coulomb radius parameter is $r_c = 1.2$. (Energy, length and cross section are quoted in MeV, F and mb.)

	V	r_0	a	W	σ_R	
					$E = 100$	$E = 160$
B	-40	1.31	0.45	-15	1760	2525
M	-100	1.22	0.5	-40	1750	2510
B'	-40	1.31	0.45	-10	1720	2465
M'	-100	1.22	0.5	-27	1700	2450

state transition for both potentials are shown in Fig. 17 and reveal a very large contribution coming from small angular momentum collisions in the case of the deep potential. Whether such a large contribution for strongly overlapping collisions is realistic we cannot tell from either elastic or inelastic experiments, but the opportunity for learning this is certainly afforded by transfer reactions. In addition to plotting the amplitude of S , which most transparently reveals the important regions of l , we have also plotted S itself in the complex plane and joined these points. The resonant behavior of the deep potential signified by the rapid rotation of the trajectory around the origin is in contrast with the shallow potential. These are potential or shape resonances like those known from neutron scattering. This behavior appears also in the elastic S -matrix, but since it is in the low- l region, where

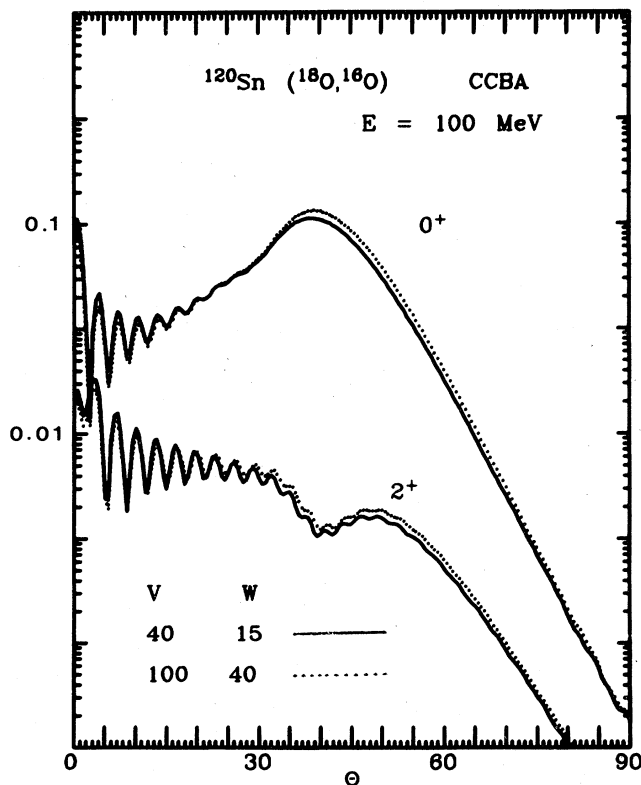


FIG. 18. Cross sections for two-neutron transfer to the ground and 2^+ vibrational state. The two cases refer to the Becchetti and Morrison potentials of Table IV. The S -matrix for the ground state transition was shown already in Fig. 9.

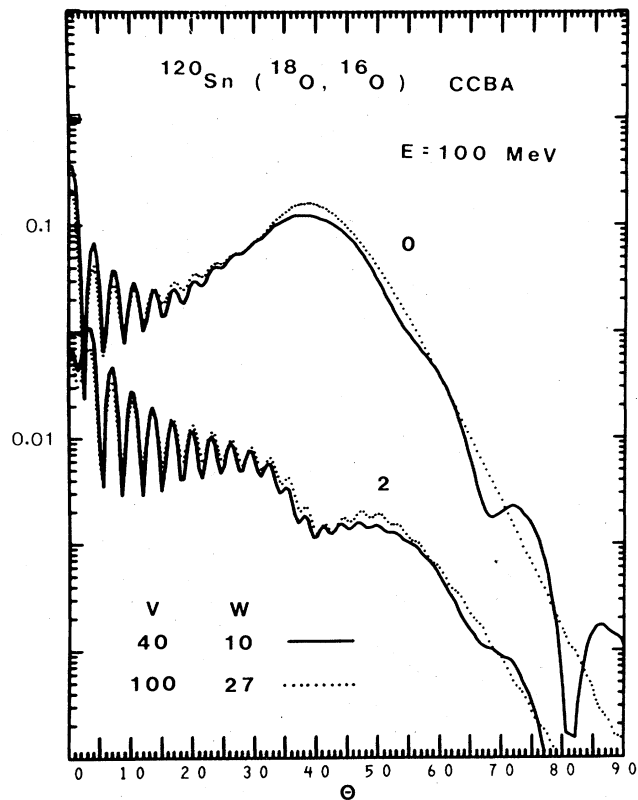


FIG. 19. Cross sections for two-neutron transfer to the ground and 2^+ vibrational state computed for the reduced absorptions indicated by potentials B' and M' in Table IV. Experiment could not easily distinguish between these.

S is several orders of magnitude less than unity, it does not manifest itself in elastic scattering, but rather in several-nucleon transfer reactions.

Perhaps it is not so surprising that such different potentials as the two compared above could be distinguished. Therefore, we turn our attention to two which are more conventional. The one is the standard that we adopted at the beginning of this article and which was the basis for the potentials of Table III. It was employed by Becchetti (Becchetti *et al.*, 1972) in the $O + Pb$ reaction. The other one is due to Morrison (1971), which he used for $O + Ca$. They are labeled B and M in Table IV. It may be noticed that the Morrison potential is very similar to one (97) in Table III, and it is not surprising therefore that they cannot be distinguished by elastic and inelastic scattering. In fact, the two-neutron transfer reaction at $E = 100$ MeV shown in Fig. 18 does not distinguish between them either. The S -matrix for the Becchetti potential was shown in Fig. 9 and reveals no interior contributions. Only a narrow band of angular momenta centered at the critical angular momentum l_c are important. Knowing that the imaginary potential is poorly determined we have reduced it for both potentials but in such a way that the reaction cross sections remain about equal for the two potentials. This roughly insures that we are dealing with equivalently absorbing potentials. They are labeled B' and M' in Table IV. All four yield indistinguishable elastic and inelastic cross sections, and even at

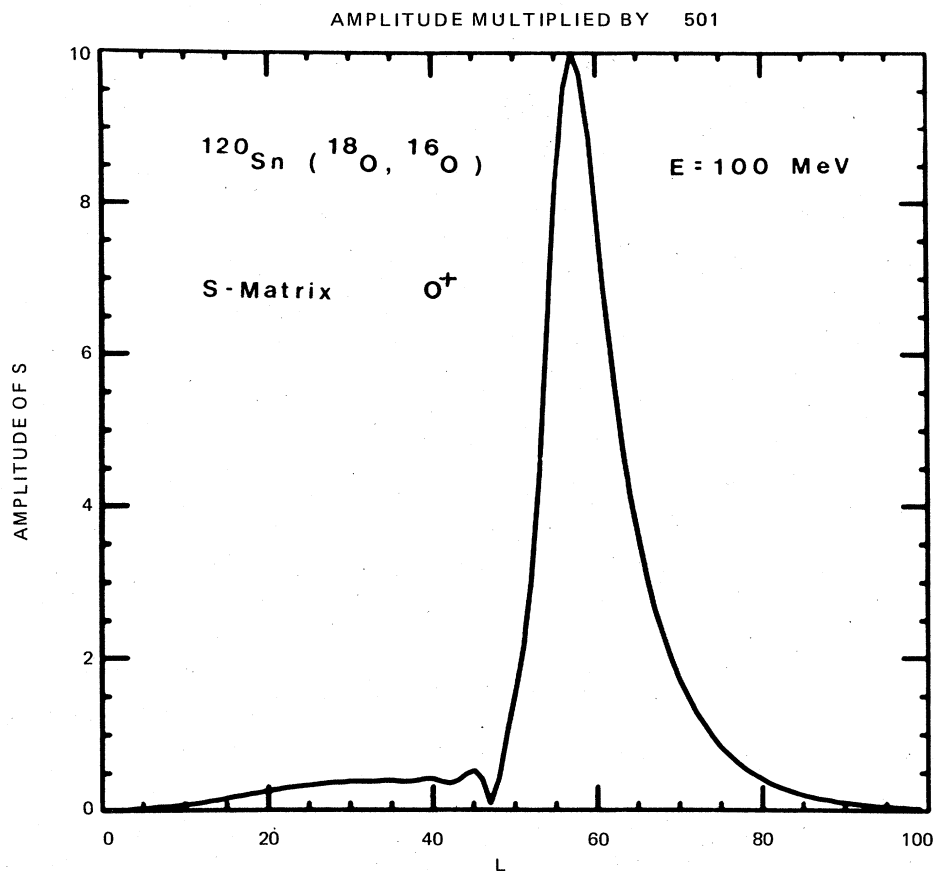


FIG. 20. Amplitude of the S-matrix for the ground state two-neutron transfer for the weaker absorbing version of the Becchetti potential ($V=40$, $W=10$). Cross section is shown in Fig. 18.

the reduced absorption we cannot distinguish easily the two-neutron transfer cross sections (Figs. 19, 20).

At this point we turn to the classical orbits to assist us in deciding what to look for that can distinguish between these two potentials. Their classical deflection functions are compared in Fig. 21 at several energies; and the penetration depths are shown in Fig. 22. It can be seen that for $l > l_c$ they give rise to the same classical cross section. However, the inner region below l_c is different in the two cases. Such differences are obscured in the quantum elastic and inelastic scattering by the imaginary potential, even when it is weak (Fig. 23). Our attention is attracted by the flat regions around $l \sim 30$ in the case of 160 MeV scattering because flat regions of the deflection function give rise to large cross sections, there being many waves that scatter near the same angle. Classically, therefore, the deep potential would produce a peak at $\theta \simeq 15^\circ$, while the shallow potential would produce a peak at $\theta \simeq 45^\circ$. Since the grazing angle, $\theta_g \simeq 23^\circ$ is so far forward at this energy, the presence of a secondary peak at 15° is likely to be obscured. However, because the cross section normally drops off quickly beyond θ_g , the secondary peak at $\theta = 45^\circ$ produced by the weak potential may be observable if absorption is not so strong as to damp altogether the interior partial waves. It turns out that for the absorption strengths originally quoted for the Becchetti and Morrison potentials, the

secondary structure is not visible. However, the two-nucleon transfer cross sections shown in Fig. 24 clearly distinguish between the deep and shallow potentials for the case of weaker absorption. In particular for the shallow potential we see the *secondary peak* at $\theta \sim 45$ as anticipated from the classical discussion. The corresponding S-matrix is shown in Fig. 25 and here we see, again in agreement with the classical picture, a subsidiary peak at $l \sim 30$. This contrasts with Fig. 9 which corresponds to the same real potential but with the stronger absorption (B of Table IV).

Thus by this consideration of classical scattering we have been led to suggest how two-nucleon transfer reactions may be used to distinguish between potentials which are equally acceptable as far as elastic and inelastic scattering are concerned. For this to be possible, however, the absorption must not be too strong (unless the real potentials are extreme, such as 308 and 5 in Table III). We note in this connection that the reduction in W shown in Table IV does not reduce the reaction cross section proportionally. We saw in Table III a selection of potentials which are equivalent for elastic and inelastic scattering. Therefore, we add that for potentials with a real depth somewhat weaker than the Becchetti potential, the secondary peak would move to larger angles, and in the reverse direction for stronger ones. The appearance in experiment of such a secondary peak would indicate that

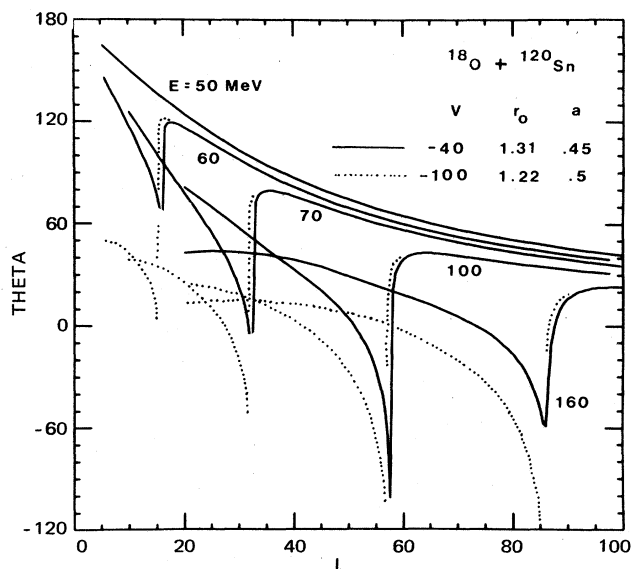


FIG. 21. Deflection functions at several energies are compared for the potentials indicated. The singularities mark the value of the critical angular momentum at each energy. The grazing angle θ_g and angular momentum l_g correspond to the maximum just above l_c in each case.

the absorption is "weak" and the real potential shallow. The absence of such a peak would be inconclusive.

We have seen in this section a sample of two-nucleon cross sections which are widely different, depending upon the potential acting between the nuclei at distances corresponding to appreciable overlap. The differences show up at angles away from the grazing angle. This is natural, of course, since the grazing angle is so called because it is only modestly perturbed by the nuclear field. A re-examination of our figures reveals how important it is to

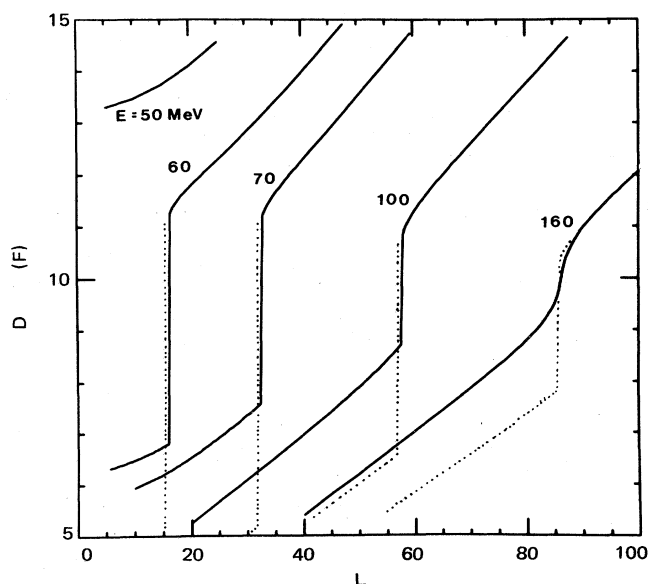


FIG. 22. Penetration depth for the two potentials corresponding to Fig. 21. Note the gradual disappearance of the discontinuity. This depends on the force near contact of the nuclei, dV/dr , not on the potential depth as this figure might be interpreted to suggest.

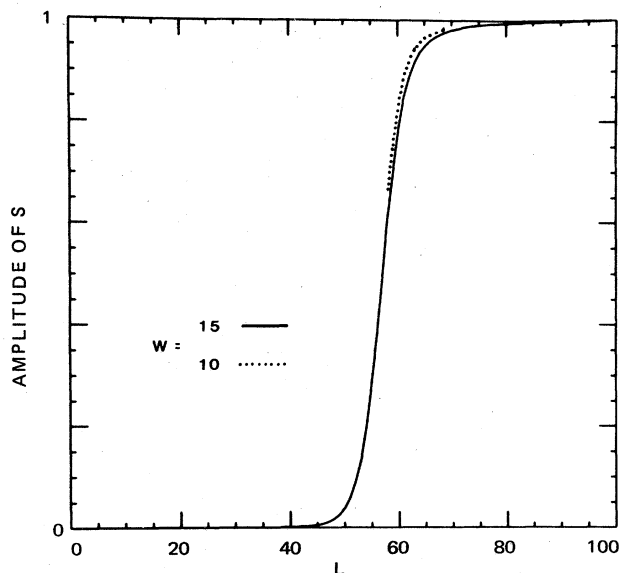


FIG. 23. Elastic S-matrix for the Becchetti potential with $W = 15$ and 10 , respectively. Even though $W = 10$ allows interior contributions to transfer reactions, the cutoff in the elastic S comes at the same l . This figure illustrates the quotation from Shakespeare.

perform measurements at small angle intervals and with good resolution and statistics. This makes the experiments slow, but they should prove very rewarding. Clearly much more information is potentially available here than in elastic or inelastic experiments. Of course, the latter play their role in defining the strength of the inelastic branch of multiple-step transfer amplitudes. But they carry very little information about the nuclear field that is unique.

I stress that the attention to two-nucleon transfer and the tin isotopes is for illustrative purposes only. For other multi-nucleon transfer reactions, and for other mass regions, the same type of classical analysis is expected to be fruitful.

VIII. QUANTAL ANALOG OF THE CLASSICAL DEFLECTION FUNCTION

In the preceding discussion we have relied heavily on the graphic aspects of classical physics to discuss heavy-ion reactions. We have also seen that the insights gained in this way are borne out, sometimes in remarkable detail, by quantum mechanical calculations (cf., Figs. 21, 23, 25). It would be useful to have criteria that would aid us in deciding under what circumstances the classical picture is a useful one. These criteria cannot be such precise ones as have been discussed elsewhere, having to do with a comparison of typical dimensions (Brogia, 1972), which are necessary but insufficient conditions. They assure us that *outside* the nuclear interaction region, classical dynamics holds approximately. But the region of most interest to us is the inside region. At least two other features are relevant. One is the effect of absorption, which, if sufficiently strong, can perturb the classical picture. Likewise, if the onset of the nuclear interaction is too abrupt over certain classical orbits, then the classical picture will be misleading for the corresponding l region. These are necessarily vague statements. However, they can be illuminated

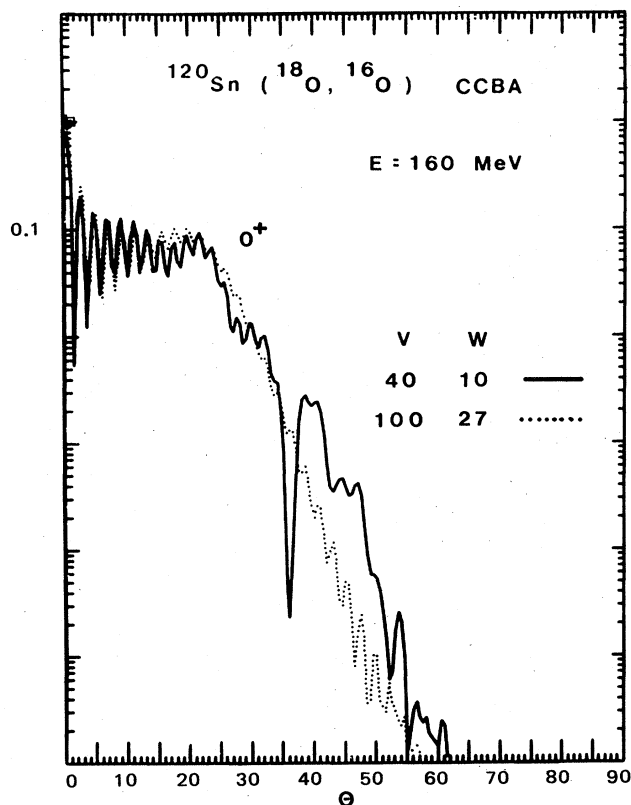


FIG. 24. Cross section for two-neutron transfer to the ground state computed at $E = 160$ MeV for the Becchetti and Morrison potential with reduced absorption (B' and M') of Table IV. Note the secondary structure in the one case occurring at $\theta = 45^\circ$ in correspondence with the classical deflection function of Fig. 21, which predicts such a peak arising from deep orbits around $l \sim 30$.

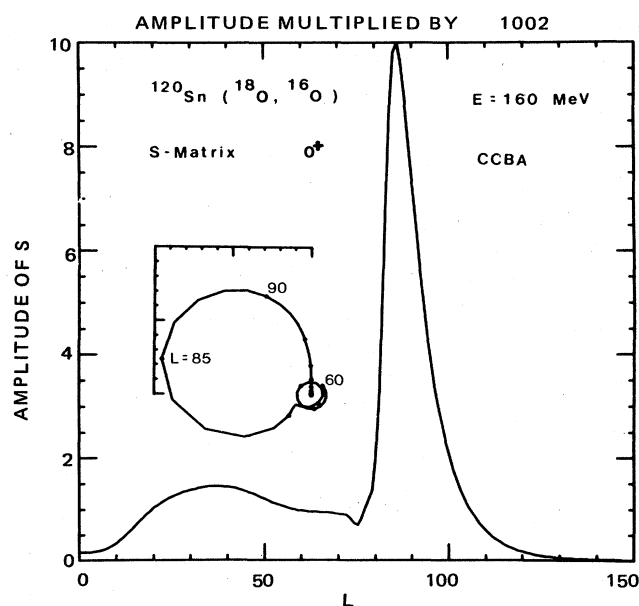


FIG. 25. S-matrix at $E = 160$ MeV for the ground state two-neutron transfer corresponding to the Becchetti potential with weak absorption (B' in Table IV). Note the broad structure around $l = 30$. Corresponding cross section is in Fig. 24. Inset shows S plotted in the complex plane from $l = 60$.

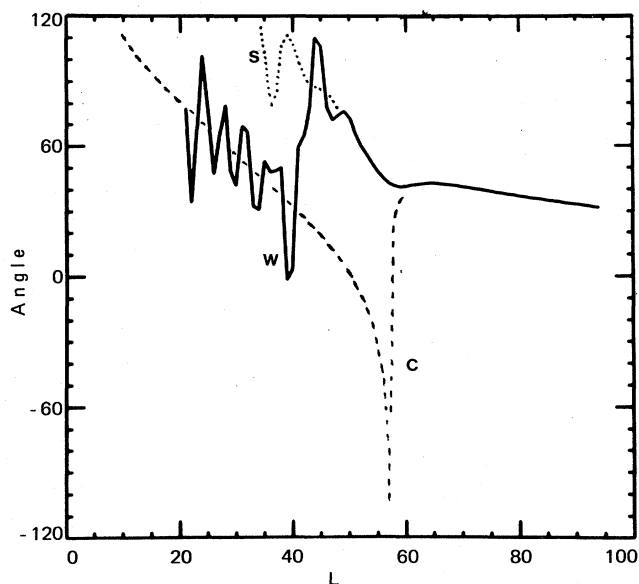


FIG. 26. The quantal deflection functions in the elastic channel for two potentials, the weak (W) and strong (S) absorbing versions of the "gentle" potential (B' and B of Table II) are compared with the classical deflection function, for $^{18}\text{O} + ^{120}\text{Sn}$ at $E = 100$ MeV.

to a considerable degree by studying what we shall refer to as the quantal deflection function.

The quantal deflection function can be obtained from the quantum mechanical expression for the scattering amplitude when the relevant partial waves are large by answering the question: for given scattering angle θ , what partial waves contribute most to the amplitude? It can be shown that the largest contribution is obtained when l has the value which satisfies the equation

$$\theta = d/dl(2\delta_{l,l} + \sigma_l + \sigma_{l'})$$

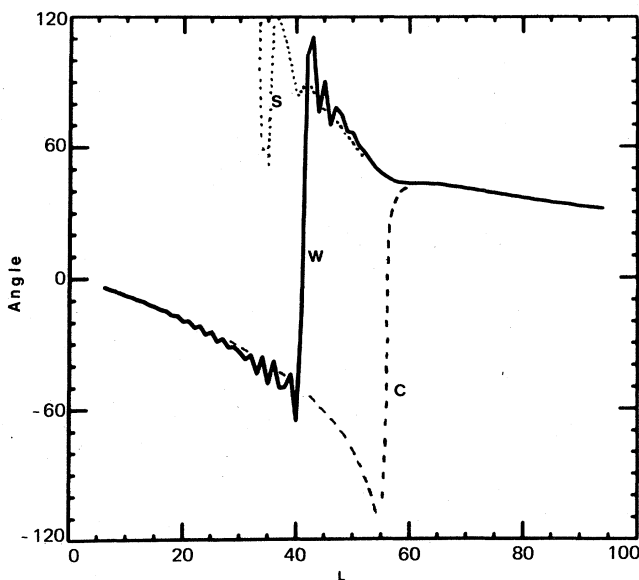


FIG. 27. The quantal deflection functions in the elastic channel for two potentials, the weak (W) and strong (S) absorbing versions of an "abrupt" potential ($V = 308$ of Table III) are compared with the classical deflection function, for $^{18}\text{O} + ^{120}\text{Sn}$ at $E = 100$ MeV.

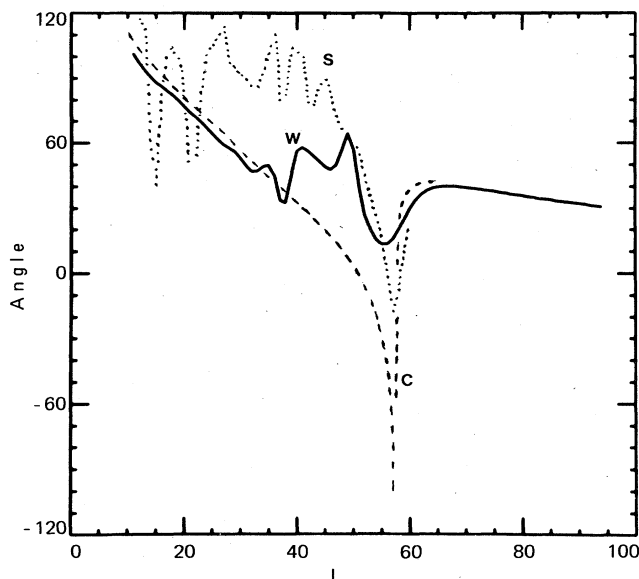


FIG. 28. The quantal deflection functions in the transfer reaction to the 2^+ state produced by $^{120}\text{Sn}(^{18}\text{O},^{16}\text{O})$ for two potentials, the weak (W) and strong (S) absorbing versions of the "gentle" potential are compared with the classical deflection function. Compare Fig. 26.

where σ_l , $\sigma_{l'}$ are Coulomb phase shifts for incident and exit channels and $\delta_{l',l}$ is defined by the corresponding S -matrix element,

$$S_{l',l} = |S_{l',l}| \exp(2i\delta_{l',l}).$$

While a similar expression was derived by Ford and Wheeler for elastic scattering, the same derivation can be applied to any reaction channel. (We classify $S_{l',l}$ by l and $\Delta l = l' - l$ so that $d\sigma_{l',l}/dl = d\sigma_{l',l}/dl'$.) The above relationship between l and θ is what we call the quantal deflection function.

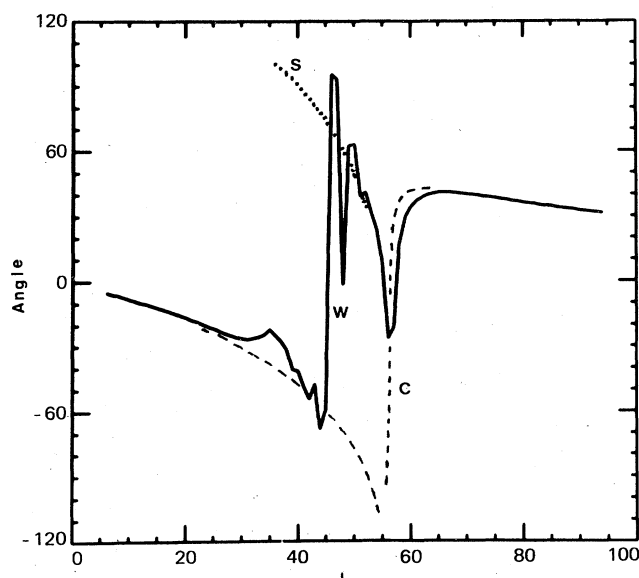


FIG. 29. The quantal deflection functions in the transfer reaction to the 2^+ state produced by $^{120}\text{Sn}(^{18}\text{O},^{16}\text{O})$ for two potentials, the weak (W) and strong (S) absorbing versions of the "abrupt" potential are compared with the classical deflection function. Compare Fig. 27.

We can easily distinguish four situations corresponding to whether the real part of the potential is "gentle" or "abrupt" and whether the imaginary part is "weakly" or "strongly" absorbing. Although we refer to potentials as being weakly or strongly absorbing, these are relative terms which distinguish whether or not direct reactions have contributions coming from the interior. Certainly all acceptable potentials which reproduce elastic data are strongly absorbing in the elastic channel in the sense that the S -matrix in this channel is small compared to unity for $l \ll l_c$ (Fig. 23): there is negligible elastic scattered flux from the interior region. In contrast, the unit of measure in reaction channels is not unity but the peak value of the corresponding S , which is small compared to unity. Figures 9 and 20 illustrate reaction S 's for strong and weakly absorbing potentials in this sense, both of which are strongly absorbing in the elastic channel (Fig. 23).

As an example of a "gentle" real potential we employ the Becchetti ($V = 40$ MeV) potential, and for strong and weak² absorption we choose $W = 15$ and 10 (potentials B and B' of Table IV). As an example of "abrupt" potentials we employ both the strong and weak absorption versions of the $V = 380$ MeV potential of Table III.

The first comparisons that we make are between the deflection functions for quantum *elastic* scattering and classical scattering. Such comparisons are shown in Figs. 26 and 27 for the "gentle" and "abrupt" potentials. In all cases we remark on the large differences between the quantal and classical deflection functions. This has been previously noted in the literature (Harney, 1974). However, we point out that this result was to be expected. The quantal elastic scattering possesses a highly non-classical aspect, the scattering into the shadow region of the black disk created by absorption.

We turn therefore instead to a comparison of quantal deflection functions computed for *reaction* channels, and in particular the two-neutron transfer channels which we have used earlier for illustration. We compare such quantal deflection functions with the classical deflection function for the "gentle" potential in Fig. 28 and for the "abrupt" potential in Fig. 29, and in each of these cases for the weak and strong absorption versions of these potentials.

For the "gentle" potential we find that strong absorption leads to a deflection function which departs radically from the classical result below the critical angular momentum, although the falloff below the grazing angular momentum reproduces the rainbow effect. On the other hand, "weak" absorption leads to a strong resemblance between the quantal and classical deflection functions except in a small region just below the critical angular momentum. Because the classical cross section is inversely

² Actually this is not such a weakly absorbing potential, as can be seen from Fig. 20 where, although there is some contribution to the reactions from low l , it is still a small one. However it will serve as an example of a weaker absorption than the strong absorption with which it is compared. It should be stressed that the absorbing power of a potential is not determined by the magnitude of the imaginary part but by the ratio of $W/(E - V)^{1/2}$ as seen from Eq. (6). Here V is the sum of nuclear and Coulomb potentials so that $E - V$ is the local kinetic energy. Also the absorption is proportional to \sqrt{M} .

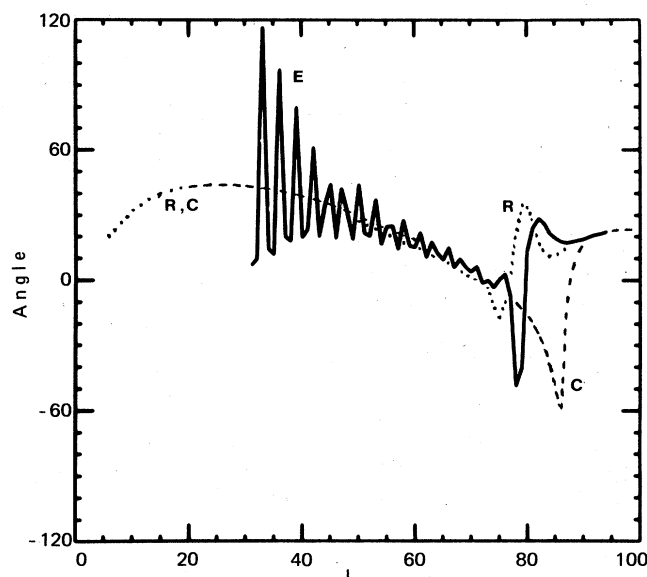


FIG. 30. The quantal elastic (E) and reaction (R) deflection functions (the latter for the $^{120}\text{Sn}(^{18}\text{O}, ^{16}\text{O})$ ground state transition) are compared with the classical (C) result for $E = 160$ MeV. This example compliments Figs. 21 and 25.

proportional to the slope of this function, the above is an unimportant discrepancy.

For the "abrupt" potential we find an interesting situation in Fig. 29. If the absorption is weak, then there is a broad band of partial waves below the critical angular momentum for which there is no correspondence between the quantal and classical deflection functions. These correspond to the classical orbits over which the real potential is too "abrupt." A wave packet built from such a band of partial waves is broken up by the nuclear potential because of the transverse force. For still lower partial waves the direction of motion and the direction of the force (which is radial) are almost the same, so that it is not dispersive. The quantal deflection function then approaches the classical result, becoming equal to it at small l .

For the fourth combination, an "abrupt" and strongly absorbing potential, the quantal deflection function differs from the classical one for all $l \lesssim l_c$. Here the abruptness of the potential is overshadowed by the strong absorption which prevents the sampling of the potential in the region where it becomes abrupt.

As a final example of the correspondence between the quantal and classical deflection functions in reaction

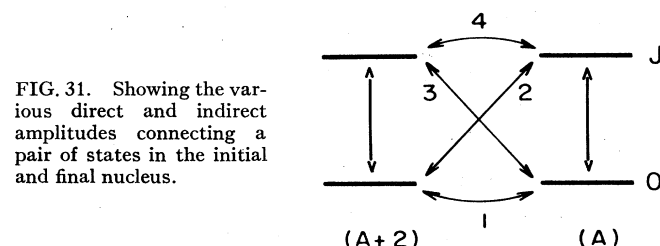


FIG. 31. Showing the various direct and indirect amplitudes connecting a pair of states in the initial and final nucleus.

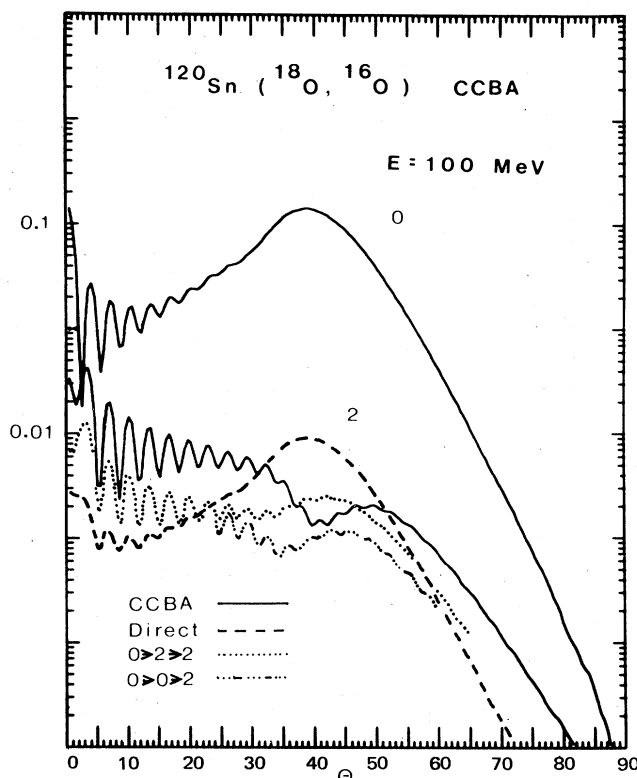


FIG. 32. Two-nucleon transfer cross section leading to the ground and 2^+ collective state shown by solid lines. For the 2^+ the direct transition (DWBA) is shown by dashed line. The other two curves are indirect transitions calculated separately. The destructive interference produces a dip at the grazing angle and a generally falling cross section compared to the grazing angle peak of the ground state.

channels we return to the example of Sec. VII where we were able to predict a specific difference in the transfer reaction cross sections depending on whether the real potential is shallow or deep. On the basis of Fig. 21, a secondary peak beyond the grazing angle was predicted for the transfer cross section at $E = 160$, corresponding to the broad flat region of the classical deflection function in the region of $l = 30$. In Fig. 30 we compare the quantal deflection functions for the elastic and two-nucleon transfer channel with the classical function. While the quantal elastic deflection function oscillates violently, the transfer deflection function corresponds exactly with the classical one except in a narrow band just below the critical angular momentum.

We conclude from the foregoing discussion that if the absorption is not too strong then the classical and quantal deflection functions for reactions correspond in regions where the transverse force acting on the orbits is not strong. In

TABLE V. Nuclear and charge deformations which are associated with the target radius parameter of $r_N = 1.12$ and $r_c = 1.2$, respectively. They were determined by proton inelastic scattering and Coulomb excitation, respectively.

	^{120}Sn	^{122}Sn	^{112}Sn	^{114}Sn
β_N	0.13	0.124	0.143	0.143
β_c	0.112	0.118	0.13	0.118

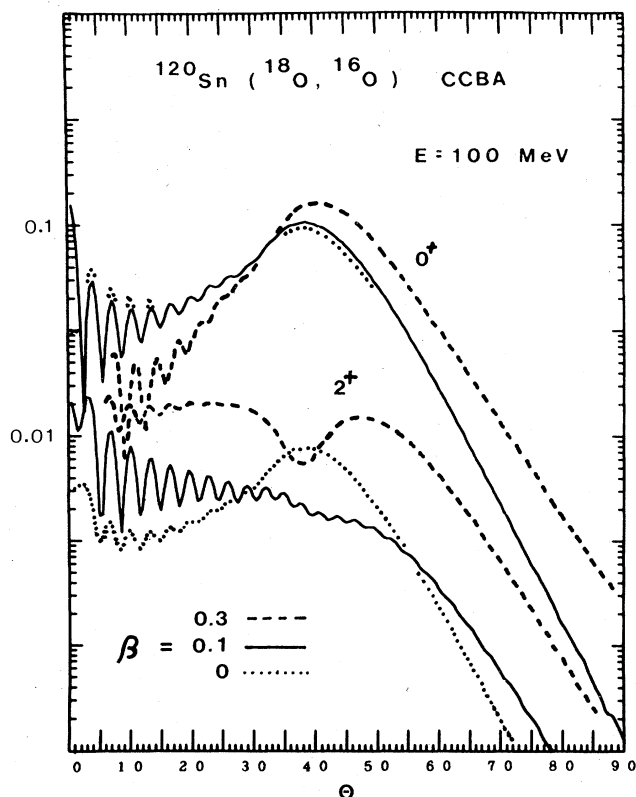


FIG. 33. The changing pattern produced by interference in producing the 2^+ is illustrated for several strengths of collectivity of the inelastic branch appearing in the indirect transitions.

practice the transverse force is too strong only for a band of orbits just below the critical one.

IX. INDIRECT TRANSITIONS IN TWO-NUCLEON TRANSFER, OPPOSITE BEHAVIOR FOR STRIPPING AND PICKUP

Nucleon transfer reactions were originally conceived as involving a direct transfer from the ground state of the target to the final state of the residual nucleus. More recently we have learned that indirect transitions involving an inelastic transition as an intermediate step, as illustrated in Fig. 24, sometimes compete in importance with the direct transition, and in certain cases can strongly modify the shape of the angular distribution. Such processes were predicted to be strong in calculations of the (p, t) pickup reaction on vibrational nuclei (Glendenning, 1969; Ascutto and Glendenning, 1970), but their first convincing appearance in experiment was observed in deformed nuclei (Ascutto, Glendenning, and Sorensen, 1971, 1972; Tamura *et al.*, 1970).

Interestingly the signature of indirect reactions connecting *vibrational nuclei* is weak for two-nucleon pickup but strong for stripping. The reason for this is that the sign of the parentage amplitude connecting the ground to a vibrational state has opposite sign for the reverse reaction (transitions 2 and 3 in Fig. 31). This implies that the direct transition (2 or 3) will interfere in the opposite sense with the second-order indirect transitions for pickup as compared with stripping. It turns out to be constructive

for pickup such as the frequently studied (p, t) reaction, and the signature is therefore weak compared to the less commonly studied stripping reactions where the destructive interference alters the angular distribution shape. This probably accounts for the very late discovery of these processes in light nuclide transfer reactions.

In heavy-ion reactions the effect of indirect transitions on two-nucleon stripping connecting vibrational nuclei is illustrated in Fig. 32 (Ascutto and Glendenning, 1973a and b). There the cross sections computed separately for the direct and the two second-order indirect transitions to the 2^+ state are shown. When all amplitudes are taken together, the cross section is very strongly altered from the grazing peaked angular distribution characteristic of the direct transition. In particular, for the strength of the inelastic transitions used here (see Table V) the interference produces a dip at the grazing angle. Of course there is a continuous evolution between the dashed and solid curve as the deformation increases from 0 to the value used. For several strengths of β the cross sections are shown in Fig. 33.

The ground state is very little affected by the indirect transitions because branches 2 and 3 of Fig. 31 are parts of the second-order indirect transitions leading to the ground state, and as mentioned earlier they have opposite signs. As a result they tend to cancel each other so that

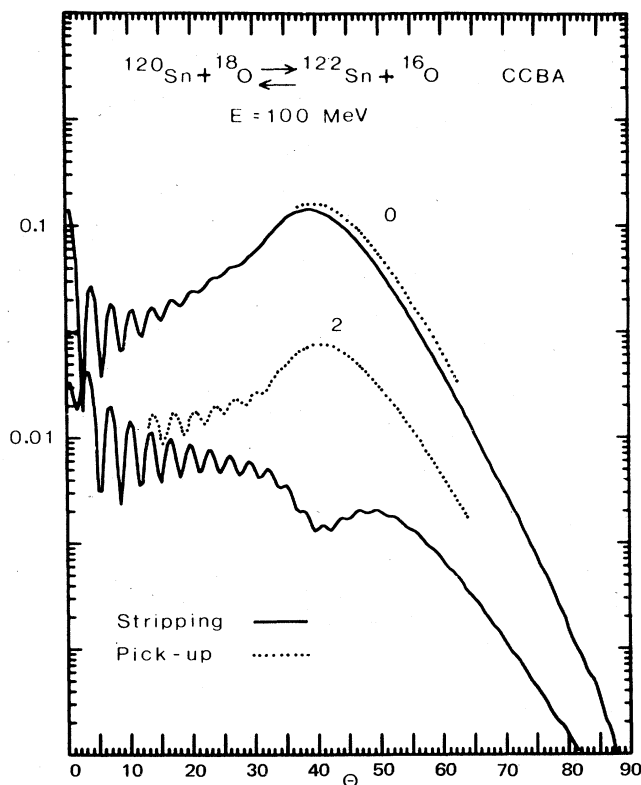


FIG. 34. The two-nucleon stripping and pickup reactions are compared. Note the marked difference of the cross sections to the two 2^+ states arising from the opposite sense in which the direct transition interferes with the indirect in stripping compared to pickup. (Ground state transitions would be time reversed if calculated at the time reversed energies.)

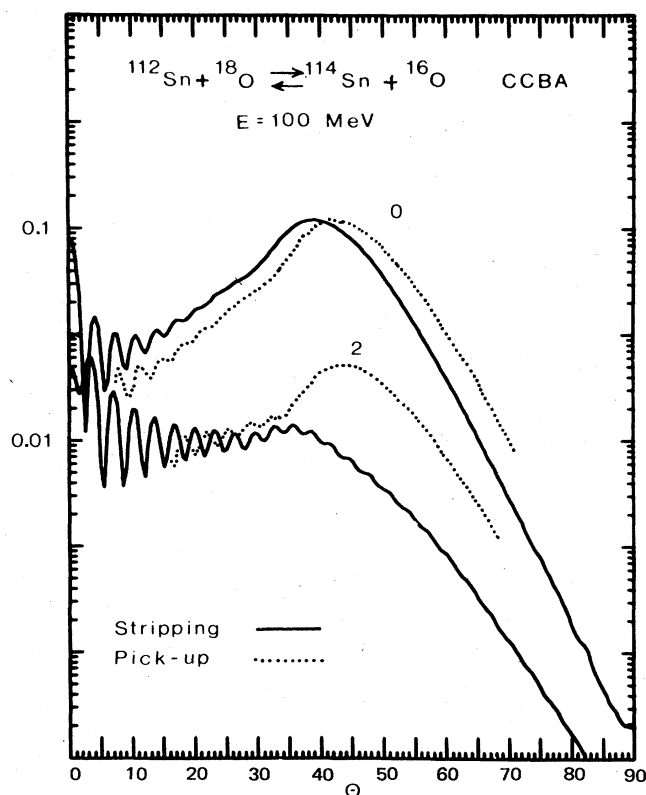


FIG. 35. Two-nucleon stripping and pickup are compared at the light end of the tin isotopes. Compare with the heavy end shown in Fig. 34.

the ground state transition in a good vibrational nucleus will be almost purely direct.

The inverse pickup reaction leading to a vibrational state contrasts (Ascutto and Glendenning, 1973) sharply with the stripping reaction as seen in Fig. 34. (The ground state transitions would be time reversed and identical if carried out at the reversed energies. Here they were done at the same bombarding energy.) A similar situation holds at the opposite end of the tin isotopes, as Fig. 35 reveals. The interference in the production of the 2^+ state is weaker, depending as it does on the details of the nuclear wavefunctions. The collective state was, for these illustrative calculations, taken to be a superposition of two quasi-particle states (Arvieu and Vénéroni, 1960a and 1960b) represented by eigenstates of a Woods-Saxon potential. The dependence on the nuclear wavefunctions is amplified by the fact that the several transfer amplitudes are comparable in magnitude and are coherent, which provides unusual sensitivity.

X. FORWARD ANGLE RIPPLES, UNCERTAINTY PRINCIPLE

A prominent feature of all the two-nucleon cross sections appearing here are the forward angle ripples or high frequency oscillations. This phenomenon is likely to be very general for heavy-ion reactions (Ascutto and Glendenning, 1973a and 1973b), for it depends on a sufficiently high localization in l . Such a localization occurs in heavy-ion transfer reactions because the reaction in r space is a ring, bounded on the inner side by absorption and on

the outside by the decay of the bound state wavefunctions. The frequency of the ripples is determined by the angular momentum l_0 corresponding to the peak in S . The angle between ripples is then $\delta\theta \cong \pi/l_0$. We have noticed that l_0 generally corresponds to the critical angular momentum l_c . If the S -matrix were a delta function $\delta(l - l_0)$ then the angular distribution would be given by $|Y_{l_0}(\theta)|^2$. The ripples will be damped as the scattering angle increases from zero according to the width Δl of S .

One can support the picture above by computing the angle $\delta\theta$, corresponding to an extra path length of one wave length between two orbits scattered to the same angle from opposite sides of the nucleus (such as orbits 2 and 3 of Fig. 3)

$$\delta\theta = \sin^{-1} \frac{\lambda}{2R} \cong \frac{\lambda}{2R} = \frac{\pi}{KR} = \frac{\pi}{l_0}$$

Of course one must use the *local* wavelength for λ because this refers to an orbit scattered through the nuclear edge (e.g., orbit 3 of Fig. 3). Doing so, one computes $\Delta\theta \cong 3^\circ$ for the $E = 100$ MeV case in agreement with the ripples.

Thus the frequency of the ripples if it corresponds to l_c provides no new information, the critical angular momentum being the one parameter that elastic scattering unambiguously provides. The existence of the ripples does

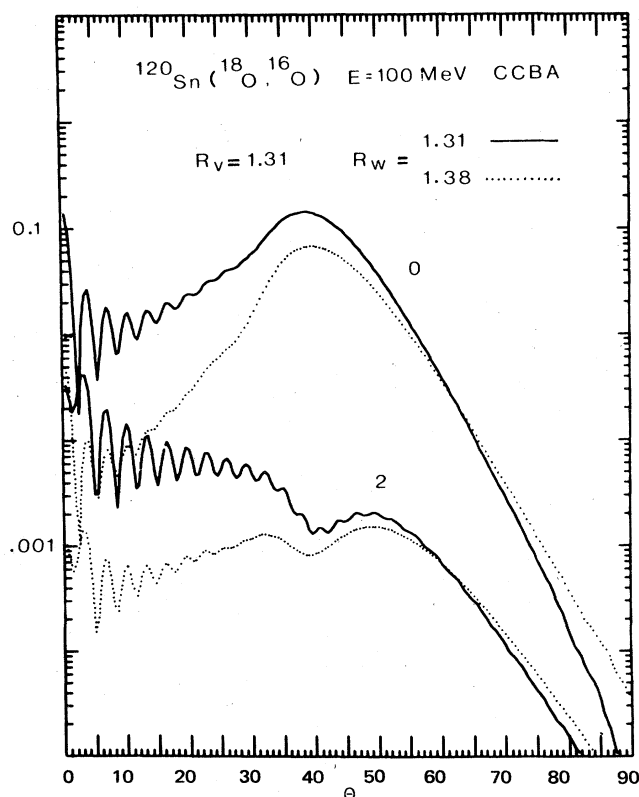


FIG. 36. Showing how the forward angle cross section relative to the grazing peak depends sensitively on the edge of the nuclear field, as illustrated here through the relationship between the radius of real and imaginary potentials.

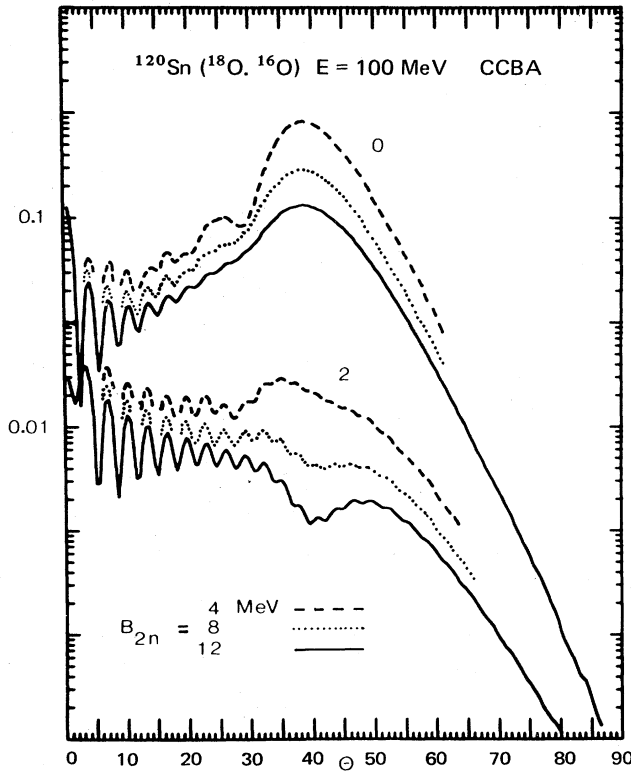


FIG. 37. Showing how the cross sections depend upon the slope of the form factor in the asymptotic region as determined by the separation energy B_{2n} of the two nucleons.

not depend, as has been suggested (Chasman, Kahana, and Schneider, 1973), on the weakness of the absorption, but rather on the localization of l space. What is of interest is the relative cross sections at the grazing angle and at forward angles as measured, say, by the envelope of the ripples. Since the forward cross section in two-nucleon transfer is particularly sensitive to the close orbits of type 2 and 3 in Fig. 3 they provide a sensitive probe of the nuclear edge, in particular the relationship of the imaginary to real potential (Fig. 36) (Ascutto and Glendenning, 1974).

It is worth noting that in the neighborhood of $\theta = 0$ the first one or two oscillations show a dependence on the angular momentum transfer (in our case $L = 2$). It would be hard to detect the difference in cases where the frequency of the ripples is so small, but at lower energy (Ascutto and Glendenning, 1973a and 1973b) or for lighter target (Henning *et al.*, 1974) it is feasible.

It may also be of interest that the forward angle ripples do in some cases reappear beyond the grazing peak (cf., Figs. 16 and 24). We consider this more likely when the grazing angle itself is far forward.

One exception to the relationship between the ripple frequency and the critical angular momentum is seen in Fig. 16 for the deep potential which has an appreciable interior contribution (Fig. 16). In this case the ripples are probably the result of a more complex interplay be-

tween the phases of different angular momenta resulting from the rapid phase changes of the S -matrix (Fig. 17) for the low- l region.

It is interesting to relate the width of the grazing angular distribution (Fig. 18) to the width of the corresponding S -matrix (Fig. 9). Reading these values at one-half the maximum value, we have $\Delta\theta \simeq 18^\circ = 18\pi/180$ radians and $\Delta l \simeq 10$. This gives

$$\Delta\theta \Delta l \simeq \pi.$$

Thus we see that the grazing peak could not be much narrower and still be consistent with the uncertainty principle.

Related to this, we show in Fig. 37 how the separation energy of the transferred nucleons affects the angular distribution. This was done by replacing the tail of the form factor in Fig. 8 by a Hankel function tail for $r > 10F$. The decay length corresponding to $B_{2n} = 12$ MeV is very close to the original. The grazing angle peak is seen to become narrower as the binding weakens, corresponding to broader S -matrices (Fig. 38). However, the sensitivity to B_{2n} is very weak, since the uncertainty in the decay length surely is less than the large variations in B_{2n} illustrated.

XI. TWOFOLD NATURE OF COULOMB-NUCLEAR INTERFERENCE

We call attention to the fact that there are actually two distinct phenomena which contribute to the so-called Coulomb-nuclear interference. One of these corresponds to a partial cancellation of the impulse delivered to the excited nucleus. The sense of the impulse along certain orbits (near the grazing one) changes sign as they pass through the Coulomb, then the nuclear, and finally the

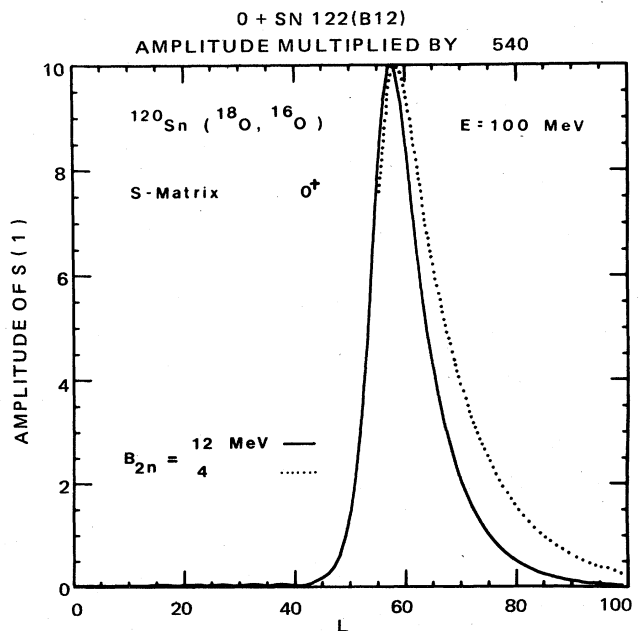


FIG. 38. The amplitudes of the S -matrix for the ground state transitions of Fig. 37 showing the broadening for weaker binding. Amplitude of dotted curve is multiplied by 282.

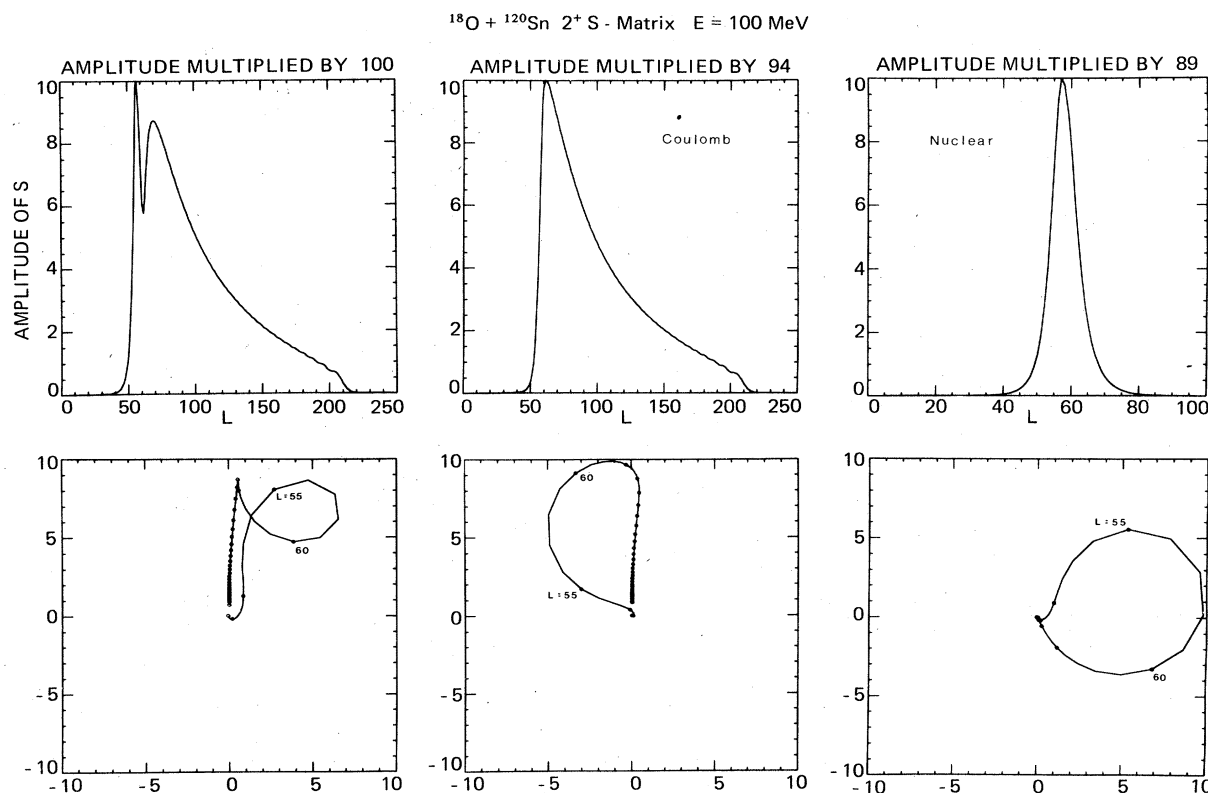


FIG. 39. For inelastic scattering to the collective 2^+ state the amplitudes of the S -matrix are shown for the complete process and for pure nuclear and pure Coulomb excitation. Below, the S -matrices themselves are plotted in the complex plane as points, which are joined. Dots mark intervals of 5 units. The vector sum of the nuclear and Coulomb parts at corresponding l yield (to lowest order) the complete S . The points corresponding to $l = 55$ and 60 are marked and the others can be located by counting. Note that the l scale for the nuclear S amplitude is expanded. In the first part of the figure, it is the spike at $l \sim 57$. Also note the slow convergence of high l as revealed by the density of points and their slow approach to the origin.

Coulomb field again. The second phenomenon arises from the interference of *different* partial waves, which in the combined nuclear and Coulomb field scatter to the same angle. Such orbits are 1, 2, and 3 in Fig. 3. The outer one feels only the Coulomb field, while the others feel the nuclear field very strongly. The orbit over which the impulse is partially canceled lies between. Both phenomena have been discussed in the literature, but it apparently has not been realized that they are distinct. The impulse cancellation can be studied in Fig. 39. There, in addition to the complex S -matrix, we have separately calculated the contributions from nuclear and Coulomb excitation arising from the two parts of the multipole field

$$F_L(r) = -\beta R \frac{\partial V}{\partial r} + \beta_c \frac{3Z_1 Z_2 e^2}{2L+1} \begin{cases} \frac{R_c^L}{r^{L+1}}, & r > R_c \\ \frac{r^L}{R_c^{L+1}}, & r < R_c. \end{cases}$$

[This is written to first order in β but can be extended to arbitrary order (Glendenning, 1967).]

Points on the Coulomb and nuclear S -matrices corresponding to the same value of l yield (to first order in the excitation) the complete S . The S are complex and not 180° out of phase. As a result the cancellation, which is not complete, can produce a twist in S as is seen. The

fact that the nuclear and Coulomb components are not 180° out of phase, as are the real parts of the multipole field, is due both to the complexity of the nuclear field and to the fact that the orbits in the two cases of pure nuclear or Coulomb excitation have different histories.

XII. STRUCTURE OF THE S -MATRIX, SPECULATIONS ON FUTURE DEVELOPMENTS

In this section I shift emphasis from the cross sections and their dependence on the physical parameters, to the S -matrices underlying the cross sections. There are several reasons why the S -matrix may prove a useful entity to study. Rather trivially it portrays the important regions of l space, and therefore tells us the interaction region. But beyond this I am motivated by two other possibilities. One concerns the direct parametrization of S , especially its high- l domain. The other concerns the development of semiquantal methods of computing S (Miller, 1970; Broglia *et al.*, 1974). In heavy-ion reactions we will sometimes be faced with the need to carry large numbers of partial waves (perhaps thousands). This is especially so for inelastic scattering because of the slow fall off of the electric field. It is also true for transfer reactions when both target and projectile are truly heavy and the energy exceeds the Coulomb barrier (hundreds of MeV). One can then imagine that it may be useful to combine a quantum calculation of S up to the region of the critical angular momentum, where the nuclear field causes rapid changes

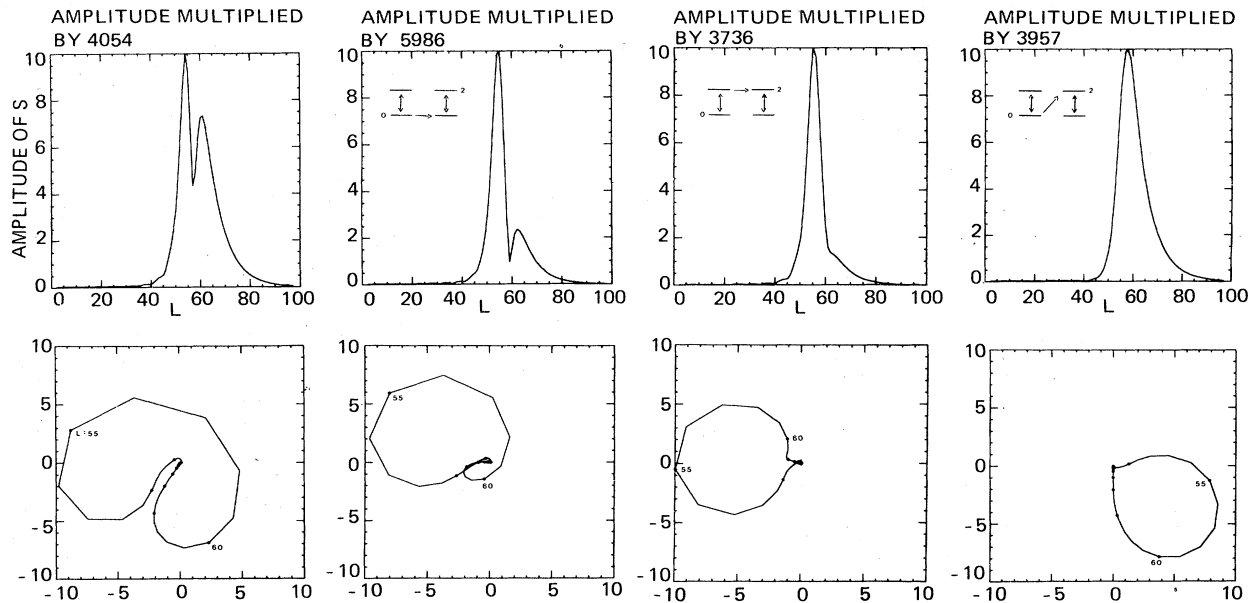
$^{120}\text{Sn}(^{18}\text{O}, ^{16}\text{O})\ 2^+\ \text{S-Matrix}\ E=100\ \text{MeV}\ \text{CCBA}$ 

FIG. 40. For two-nucleon transfer to the 2^+ state the amplitude of the S -matrix is shown together with the contributions from the direct and two second-order indirect routes (Fig. 31). The minimum near $l = 57$ is produced by the destructive interference between the two indirect terms with the direct. This is evident from the plots showing S in the complex plane. The complete S is (to high accuracy) the vector sum of the last three. Points corresponding to $l = 55$ and 60 are indicated.

in the deflection function (Fig. 6), with one of the other methods for the high- l region, where the conditions for classical scattering are more closely fulfilled. In the high- l region the phase and the amplitude of S are very smooth and slowly changing functions of l so that the possibility of interpolating S between calculated values at widely spaced intervals also exists. This last point can be illustrated in Fig. 17, where, in one case, even though the region below l_c manifests resonant behavior, nevertheless S becomes a slowly varying and orderly function of l . While this particular calculation was no problem, for truly heavy projectiles the density of l points on these figures is enormously magnified and a fully quantum calculation of each contributing l would be very costly.

The S -matrix for inelastic scattering provides another example (Fig. 39). The complete S -matrix which has a *twist* appears to be very complicated until it is realized that, to lowest order in the excitation (DWBA), it is the vector sum of the two simple loops shown for pure Coulomb and nuclear excitation. The twist occurs because of the opposite sense of the nuclear and Coulomb fields. Also in some cases the nuclear S may exhibit resonant behavior analogous to that shown in Fig. 17. In any event the two-part approach would be warranted, consisting of a fully quantum calculation of the low- l region and a parametrization or semiquantal calculation of the high- l region. For the high- l region, interpolation between widely calculated l 's can also be exploited. In this connection we note that the amplitude of S beyond the second peak, i.e., the Coulomb part, is roughly proportional to

$$S_l \propto 1/D(l)^3,$$

where $D(l)$ is the turning point on the classical orbit l .

This corresponds to the r dependence of the quadrupole field and provides a useful interpolation formula.

Nucleon transfer reactions, where multiple-step processes are important, present a special problem because of interference. The amplitude of S for the 2^+ state produced in the two-nucleon transfer reaction is shown in the first part of Fig. 40. The minimum occurring near l_c arises from the interference of direct and two second-order amplitudes, also shown. This interference produces the unusual two-lobed figure when S is plotted in the complex plane. (Third- and higher order contributions are included in the complete calculation but are much smaller than second and first order.) The indirect amplitudes, which peak at a slightly lower l than the direct, plunge precipitously above the peak, but then exhibit a shoe. This mirrors the Coulomb excitation amplitude (Fig. 39) reduced in strength and cutoff much more rapidly by the particle transfer process, which cannot occur with appreciable probability when the distance separating the nuclei is too large. The rapid convergence of the particle transfer process, even when receiving contributions from Coulomb excitation, was correctly predicted prior to the calculations (Ascutto and Glendenning, 1972) and was decisive in encouraging us to carry out fully quantal calculations (Ascutto and Glendenning, 1973a and 1973b). The shoe occurs just in the region where the interference between the nuclear and Coulomb fields produces a twist in the inelastic S -matrix (Fig. 39), and accounts for the kinks near the ends of the indirect S -matrices. To a high degree of accuracy, the complete S -matrix is the sum of the individual amplitudes. (The inaccuracy enters at the third order of the inelastic transitions.) Using whatever methods seem appropriate for calculating the separate components

of S and their low- and high- l regions, the unusual two-lobed S -matrix characterizing the complete transition can be obtained.

XIII. SUMMARY

I have reviewed the aspects of classical scattering that are useful in understanding the dependence of heavy-ion reactions on the physical quantities governing the interaction. I emphasized how classical scattering can be used to suggest how to choose experiments that may be decisive in answering specific questions. When classical scattering is used in conjunction with quantum calculations, we are in a position to understand the reactions in detail not previously attained in nuclear physics.

We saw a variety of different angular distributions for two-nucleon transfer (typical, I believe, of multi-nucleon transfer) depending upon the assumptions made about the interaction region corresponding to an interpenetration of the two nuclei. To answer the outstanding questions about this region and the dynamics of the reaction for these collisions, we require a wealth of experimental data taken at angles both forward and back of the grazing angle, and at close angular intervals so as not to miss sharp minima. I do not underestimate the difficulty of doing such experiments. I hope I do not overestimate their importance.

The structure of the S -matrix, both as a function of l and decomposed into separate components corresponding to specific processes, provides valuable insights. For reactions in which many hundreds of angular momenta are involved, a two-part approach to the calculation of the S -matrix was suggested, employing quantum mechanics for the region where the nuclear force is dominant and semiclassical or semiquantal methods for the high- l region, where the smooth behavior of S even permits an interpolation between widely spaced l 's.

We can look forward with enthusiasm to a period of exciting growth in our understanding of these reactions. This growth will involve developments in both our theoretical and experimental apparatus.

ACKNOWLEDGMENTS

I take pleasure in thanking many colleagues for discussions of various aspects of this work, R. J. Ascutto of Yale, B. G. Harvey, W. D. Myers, M. A. Nagarajan, and W. J. Swiatecki of the Lawrence Berkeley Laboratory, and R. da Silveira of the Institut de Physique Nucléaire, Orsay.

APPENDIX

All our quantum calculations were carried out in the coupled channel Born approximation (CCBA) (Penny and Satchler, 1964; Ascutto and Glendenning, 1969). The S -matrix elements were obtained in a coupled representation. Because we do not include effects of projectile excitation, and use always even projectiles (spin zero), the coupling scheme may be denoted by the *ket*

$$|(l_j)IM\rangle,$$

where l is the orbital angular momentum, J is the angular momentum of a nuclear state, and I is their vector sum, the total angular momentum of the system. The S -matrix elements are therefore

$$\langle(l_f J_f)IM|S|(l_i J_i)IM\rangle$$

which are independent of M . The way in which they are obtained is given by Ascutto and Glendenning (1969). In the case of an even target, $J_i = 0$, and the relevant elements are

$$\langle(l_f J_f)l_i|S|(l_i 0)l_i\rangle.$$

Thus for $J_f = 2^+$, $l_f = l_i$, or $l_i \pm 2$. Of the three elements corresponding to 2^+ states, we always showed only one, $l_f = l_i$, it being typical.

The connection of the above elements with any other coupling scheme is obtained straightforwardly by recoupling. For example, in an uncoupled scheme,

$$\begin{aligned} \langle l_f m_f J_f M_f | S | l_i m_i J_i M_i \rangle \\ = \sum_{IM} C_{m_f M_f M}^{l_f J_f I} C_{m_i M_i M}^{l_i J_i I} \langle (l_f J_f)IM | S | (l_i J_i)IM \rangle. \end{aligned}$$

This is the scheme usually employed in DWBA. If the coupling to other channels is neglected, S equals, within a multiplicate factor, a DWBA partial wave integral.

For nonelastic transitions, S and the T matrix are proportional. Sometimes other names and notations are used, such as reaction matrix, which are related by no more than factors. The scattering amplitude can be computed from the S -matrix or R -matrix, as indicated in Ascutto and Glendenning, 1969.

We saw above that for spin zero target and projectile, S depends upon l_i , l_f , and J_f . We classify the S -matrix according to l_i and $\Delta l = l_f - l_i$, and it is the $\Delta l = 0$ elements that we plot. This is also true of the quantal deflection function. Thus for a 2^+ state there are three such functions, which are very similar. We showed only those with $\Delta l = 0$ since they are typical.

REFERENCES

- Arvieu, R., and M. Veneroni, 1960a, C. R. Acad. Sci. (Paris) **240**, 992.
- Arvieu, R., and M. Veneroni, 1960b, C. R. Acad. Sci. (Paris) **252**, 670.
- Ascutto, R. J., and N. K. Glendenning, 1969, Phys. Rev. **181**, 1396.
- Ascutto, R. J., and N. K. Glendenning, 1970, Phys. Rev. C **2**, 1260.
- Ascutto, R. J., and N. K. Glendenning, 1972, Nucl. Phys. A **188**, 185.
- Ascutto, R. J., and N. K. Glendenning, 1973a, in Symposium on Heavy Ion Transfer Reactions, Argonne, Illinois (AEC Rept. CONF 730313-P1), p. 513.
- Ascutto, R. J., and N. K. Glendenning, 1973b, Phys. Lett. B **45**, 85.
- Ascutto, R. J., and N. K. Glendenning, 1973c, Phys. Lett. B **47**, 332.
- Ascutto, R. J., and N. K. Glendenning, 1974, Phys. Lett. B **48**, 6.
- Ascutto, R. J., N. K. Glendenning, and B. Sorensen, 1971, Phys. Lett. B **34**, 17.
- Ascutto, R. J., N. K. Glendenning, and B. Sorensen, 1972, Nucl. Phys. A **183**, 60.
- Bechetti, F. D., D. G. Kovar, B. G. Harvey, J. Mahoney, B. Mayer, and F. G. Pühlhofer, 1972, Phys. Rev. C **6**, 2215.
- Blair, J. S., 1957, Phys. Rev. **108**, 827.
- Brogia, R. A., and A. Winther, 1972, Phys. Rep. **4C**, 155.
- Brogia, R. A., S. Lansdowne, R. A. Malfliet, V. Roslkin, and A. Winther, 1974, Phys. Rep. **11C**, 2.
- Chasman, C., S. Kahana, and M. J. Schneider, 1973, Phys. Rev. Lett. **31**, 1074.
- Ford, K. W., and J. A. Wheeler, 1959, Ann. Phys. (N. Y.) **7**, 259.

- Glendenning, N. K., 1967, in *Proceedings of the International School of Physics Enrico Fermi, Course XL* (Academic, New York, 1969), p. 332.
- Glendenning, N. K., 1969, in *Proceedings of the International Conference on Properties of Nuclear States*, edited by M. Harvey (University of Montreal Press), p. 245.
- Harney, H. L., P. Braun-Munzinger, and C. K. Gelbke, 1974, *Z. Phys.* **269**, 339.
- Henning, W., D. G. Kovar, B. Zeidman, and J. R. Erskine, 1974, *Phys. Rev. Lett.* **32**, 1015.
- Miller, W. H., 1970, *J. Chem. Phys.* **53**, 1949.
- Miller, W. H., 1974, *Adv. Chem. Phys.* **25**, 69.
- Morrison, G. C., 1971, *J. Phys. (Paris)* **32**, Suppl. to No. 11-12, 69.
- Penny, S. K., and G. R. Satchler, 1964, *Nucl. Phys.* **53**, 145.
- Randrup, J., W. J. Swiatecki, and C. F. Tsang, 1975, private communication; LBL 3603.
- Shakespeare, W., 1599, *Romeo and Juliet*, Act III, Scene 1.
- Tamura, T., D. R. Bes, R. A. Broglia, and S. Lansdowne, 1970, *Phys. Rev. Lett.* **25**, 1507, and Errata, 1971, *Phys. Rev. Lett.* **26**, 156.